Micromechanical Finite Element Model for Constitutive Elastoplastic Analysis of Unidirectional Fiber-Reinforced Composites

by

Lucie Parietti

Thesis submitted to the Faculty of the

Virginia Polytechnic Institute and State University

in partial fulfillment of the requirements for the degree of

Master of Science

in

Engineering Mechanics

APPROVED:

O. H. Griffin, Jr., Chairman

M. W. Hyer

E. R. Johnson

August, 1994

Blacksburg, Virginia

.2

MICROMECHANICAL FINITE ELEMENT MODEL FOR CONSTITUTIVE ELASTOPLASTIC ANALYSIS OF UNIDIRECTIONAL FIBER-REINFORCED COMPOSITES

by

Lucie Parietti

O. H. Griffin, Jr., Chairman

Engineering Science and Mechanics

(ABSTRACT)

A micromechanical finite element model to compute the overall instantaneous stiffness of fiber-reinforced composites in elastic-plastic response is presented. The model is applicable to a periodic diamond array of elastic circular fibers embedded in an elastoplastic matrix subjected to a plane stress loading. This model enforces symmetry and anti-symmetry conditions isolating the smallest unit cell and should greatly increase the speed of doing "built-in" micromechanics within a larger finite element program because of the small number of degrees of freedom (12 to 14 d.o.f.). The matrix plastic behavior is modeled using the endochronic theory without a yield surface. Various off-axis elastoplastic characteristics predicted by the mini grid for a boron/aluminum composite are presented. Comparison with experimental data and a fine grid finite element solution shows very good agreement and demonstrates the effectiveness of the mini model presented.

Acknowledgements

I would like to thank my advisor, Dr. O. H. Griffin, Jr., and his post-doctoral student Dr. S.-Y. Hsu, for their guidance and encouragement.

I am very grateful to Dr. M. W. Hyer and Dr. E. R. Johnson for serving on my advisory committee and reviewing the manuscript.

I would also like to thank my mother who encouraged me to pursue a M.S. degree in the U.S.A. and my fiancé Eric who has always showed confidence in my capability.

Table of Contents

List of Illustrations

List of Tables

1. Introduction and Background

Even though overall elastic behavior of fiber-reinforced composites is reasonably well understood, elastic-plastic behavior is still under investigation. Fibrous composites exhibit significant non-linear stress-strain behavior under off-axis loading. This non-linearity is mainly due to the matrix, while the fibers are in general linear elastic up to rupture. Studying this non-linear behavior is crucial since the strain at which many common matrix materials deform plastically is well below fiber failure. Therefore, a good design must exploit the fact that a composite can carry loads even after yielding has occurred.

Several researchers have investigated the inelastic behavior of unidirectional fibrous composites. Two different approaches have been used: a macromechanical and a micromechanical approach. In the macromechanical approach, the composite is regarded as a "mixture" of two different materials and approximated as a macroscopically homogeneous medium. Although this approach is usually simpler, it often heavily relies on experimental data. Examples of such approaches are given in [1-8]. On the other hand, the micromechanical approach regards the composite as a non-homogeneous structure. This approach allows modeling more complicated composite behavior and reducing testing needs by taking internal interaction into account.

Several analytical micromechanical models were developed first. The composite cylinder assemblage (CCA) model was introduced by Hashin and Rosen [9] who derived bounds and expressions for the effective elastic moduli of fiber-reinforced composites using a variational method. In this approach, the composite microstructure is modeled as a system of cylindrical fibers embedded in a continuous matrix phase. Later, Dvorak and Rao [10] used the CCA model to derive closed-form solutions of the elastic-plastic response of fiber-reinforced composites under axisymmetric loads. Comparison with finite element plastic solutions shows the accuracy of their results. However, their model is restrictive because of the nature of the loads applied.

Another popular model which was also first used for the elastic range and then applied to elastic-plastic analysis is the self-consistent model (SCM). First devised by Hershey [11] as a means to model the behavior of polycrystalline materials, the SCM, which is based on the solution of an elastic ellipsoidal inclusion problem [12], was extended later to multiphase media [13-14]. This model is very simple, but it takes great liberties with the geometry and gives inaccurate results for some quantities. When a variant of the self-consistent scheme is used to study elastic-plastic response of fibrous composites, it overestimates the initial yield stress [15] and underestimates plastic strains in the early stages of deformation [16].

Dvorak and Bahei-El-Din [17] used a micromechanical model consisting of elastic filaments of vanishingly small diameters in an elastic-plastic matrix. Analytical expressions for overall compliances of the composite in terms of the phase properties and the volume fraction were derived. However, at higher fiber volume fractions, this model provides an estimate of the flow stress in transverse tension response which is rather low.

Aboudi [18] analyzed a square unit cell consisting of four square subcells (a fiber subcell and three matrix subcells), in each of which uniform stress and strain are presumed; the fibers are assumed to be arranged throughout a periodic square model (PSM). According to Hsu [19], this model can be viewed as an assembly of four non-conforming linear triangular finite elements, and thus a much more concise formulation and programming than those found in the literature can be achieved. Moreover, Aboudi's model leads to an indeterminate displacement field when the applied load involves transverse shear [20], which is ascribable to the non-conforming elements. Aboudi further derived a system of closed-form constitutive equations [21], which has been applied by Pindera *et al.* [22] to simulate inelastic behavior of a boron/aluminum composite, and by Arenburg and Reddy [23] to analyze metal-matrix laminates. However, the use of the closed-form relations is not numerically more advantageous than the usual finite element procedure for the simple triangular elements. In addition, the system of closed-form equations is not suitable for the tangential stiffness method, either at the micromechanical level or at the macromechanical level.

More recently, Sun and Chen [24] developed a micromechanical model consisting of three rectangular subcells (a fiber subcell and two matrix subcells) to calculate off-axis responses of fibrous composites. This model is very simple and can be implemented easily, but, like Aboudi's model, it does not allow modeling of matrix property gradients. Besides, both models are only applicable to a periodic square array of fibers, and it is known that significant differences in inelastic predictions exist between the periodic square (PSM) and the hexagonal (PHM) models [19]. The PSM seems too compliant for off-axis responses at small fiber angles and too stiff at large fiber angles. Therefore, no matter how the matrix material parameters are adjusted, it is impossible to obtain

reliable results for both cases. This suggests that the PHM is more suitable for modeling internal constraint hardening than is the PSM.

Finally, some authors [25-27] have used the finite element method in a conventional way to analyze small representative volume elements (R.V.E.) of unidirectional composites in the elastoplastic range. If effective behavior of composites is of primary interest and computational efficiency is a serious concern, modification of the conventional finite element implementation is necessary to meet the following requirements: (1) the smallest number of degrees of freedom (d.o.f.) used for the smallest R.V.E., (2) efficient imposition of micromechanical boundary conditions, (3) efficient computation of macromechanical variables such as average strains and stresses. The periodic hexagonal array (PHA) model developed by Dvorak and Teply [28 and 29] seems to be the only mini finite element model that satisfies the above requisites. The PHA model is capable of predicting the three-dimensional instantaneous stiffness of a composite, and uses 18 d.o.f. for three-dimensional strain-controlled simulation. However, the model approximates the fibers as hexagonal cylinders; it will be shown that the geometry of the fibers has a great influence on effective inelastic behavior of composites. In particular, significant differences in effective properties exist between models using hexagonal and circular fibers. Moreover, further reduction for the PHA model is needed to promote its computational performance for the important plane stress loading, but the derivation to the current form of the model is already lengthy [28].

The objective of this thesis is to develop an efficient micromechanical finite element model for elastic-plastic analysis of unidirectional fiber composites under plane stress loading. Recently, a micromechanical finite element model involving 318 degrees of freedom has been used by Hsu [19] for elastoplastic analysis. Good agreement has been demonstrated between the predictions of Hsu's model and experimental results provided by Becker *et al* [30] for various elastoplastic characteristics. Therefore, Hsu's model will be used as a reference, and the aim of this work is to develop a mini model involving considerably fewer degrees of freedom (almost 30 times less) but capable of predicting the same effective properties. The number of degrees of freedom of the mini model is expected to be conveniently adjustable according to composite deformation characteristics which are determined by factors such as differences in constituent stiffnesses, incompressible matrix plasticity, and radial property gradients in the matrix. To meet the aforementioned requirements for mini models, a specialized finite element implementation is needed. Nevertheless, we attempt to keep our formulation simple and its computer implementation convenient.

In Section 2.1, we first isolate a repeating element (unit cell) that will be used to model the entire lamina. In order to facilitate the extraction of macroscopic stress-strain relations, the displacement field is decomposed into a macroscopic and a microscopic component. This decomposition is described in Section 2.2. Boundary conditions that enforce periodicity, symmetry and anti-symmetry

conditions on the sides of the unit cell are summarized in Section 2.3. In the plastic range, volumetric changes are negligible with respect to other deformations. If overly restrictive interpolation functions are used in the finite element analysis, large deformations without volumetric changes are not possible. This can cause the grid to lock and grossly overestimate the equivalent stiffnesses. In our case, this phenomenon is more likely to arise because we try to minimize the number of d.o.f. Before attempting any plastic implementation, which is rather strenuous, we can use a procedure to test the grid's immunity to locking by simulating constant volume deformations within the elastic range. This procedure is described in Section 3. In Section 4, the mini grid development is presented. Section 5 describes the plasticity model used for the matrix and summarizes the iterative procedure used to perform the plastic implementation. Finally, several elastoplastic stress-strain characteristics predicted by our model for a boron/aluminum composite are presented in Section 6 and compared to Hsu's results.

2. Modeling

As mentioned earlier, our goal is to develop a mini model to predict the effective properties of a unidirectional fiber-reinforced lamina under plane stress loading.

As shown in Fig. 1, the lamina in the plane $x_1 - x_2$ is subjected to plane stress loading. The fibers are aligned with the x_1 direction and assumed to be arranged in a periodic diamond array. Both the fibers and the matrix are assumed orthotropic; the fibers are elastic, while the matrix is elastoplastic. Perfect bonding is assumed between fiber and matrix.

The fibers are assumed to be very long so that the problem is independent of x_1, the coordinate in the fiber direction. Therefore, we only need to analyze a section of our lamina in a plane parallel to the $x_2 - x_3$ plane. Note that this section is perpendicular to the loading plane.

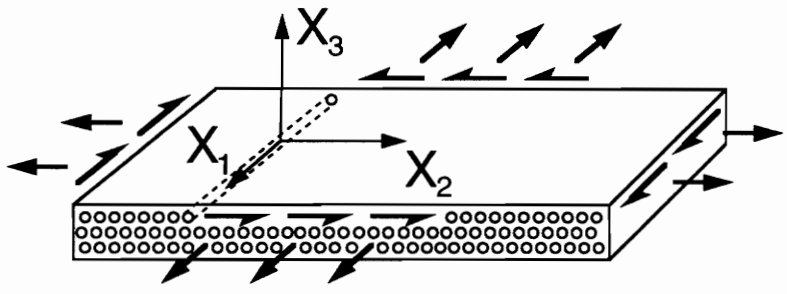

Figure 1. Plane stress loading conditions and axis system.

2.1. Unit cell

The geometry of the array (Fig. 2) is defined by the fiber diameter d_f, and the fiber spacings h and e. The fiber volume fraction v_f can be expressed in terms of these 3 parameters as $v_f = \Pi d_f^2/8eh$. Because of the assumed periodicity, a typical repeating hexagonal region can be isolated as indicated by the solid lines in the figure. Furthermore, because of the symmetry about AB and BC, only one quadrant ABCDM of the repeating unit region needs to be analyzed. This quadrant constitutes our unit cell. It represents by itself the entire composite if proper boundary conditions are applied (see Section 2.3). With M defined as the center of the rectangle BCB'C', the sloping edge AMD is defined by the angle α which can take any value as long as line AMD lies entirely in the matrix phase.

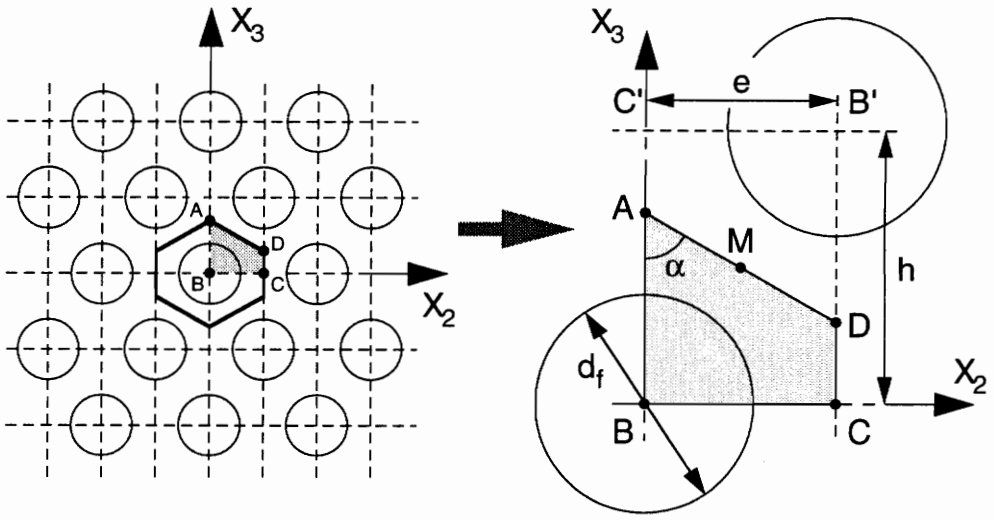

Figure 2. Unit cell.

2.2. Displacement Field Decomposition

At the macroscopic level, the composite is considered as a homogeneous orthotropic material undergoing deformations represented by a macroscopic strain field

$$\epsilon^o = \{\varepsilon^o_{33}, \varepsilon^o_{11}, \varepsilon^o_{22}, 2\varepsilon^o_{12}\}^T, \tag{1}$$

consistent with the plane stress loading conditions in the $x_1 - x_2$ plane. Note that the engineering macrostrains $\boldsymbol{\epsilon}^\circ$ are arranged in this unusual order only to make the computer implementation easier (see Section 2.4). The gradients of the macroscopic strain field are assumed to be small so that $\boldsymbol{\epsilon}^\circ$ can be considered constant across several unit cells. With this assumption, the micromechanical displacement field $\mathbf{u}$ in the unit cell can be seen as the superposition of two fields. One field corresponds to the macroscopic strain field $\boldsymbol{\epsilon}^\circ$, and the other represents a perturbation $\tilde{\mathbf{u}}$ from that state of uniform deformation due to the nonhomogeneity at the microscopic level. The displacement field $\mathbf{u}$ is thus

$$\mathbf{u} = \tilde{\mathbf{u}} + \mathbf{X}\boldsymbol{\epsilon}^\circ, \tag{2}$$

where $\mathbf{X}$ is a matrix containing the spatial coordinates (x_1,x_2,x_3) of the point where the displacement field is evaluated, i.e.:

$$\mathbf{X} = \begin{bmatrix} 0 & x_1 & 0 & x_2 \\ 0 & 0 & x_2 & 0 \\ x_3 & 0 & 0 & 0 \end{bmatrix}. \tag{3}$$

The perturbation field $\tilde{\mathbf{u}}$ will be referred to as the *fluctuating displacement field*. Since the fibers are very long, the fluctuating displacement field does not depend on the coordinate x_1 in the direction of the fibers.

2.3. Boundary Conditions

Boundary conditions are imposed on the fluctuating displacements $\tilde{\mathbf{u}}$ and the tractions $\mathbf{t}$ on the sides of the unit cell to account for the periodicity, symmetries and antisymmetries of the geometry and deformations. They are discussed in detail in [19]. We only give here a brief description. The components of the fluctuating displacement vector $\tilde{\mathbf{u}}$ in the direction of axes x_1 and x_2 (i.e. $\tilde{u}_1$ and $\tilde{u}_2$, respectively) are anti-symmetric about the $x_1 - x_3$ planes at $x_2 = 0$ and $x_2 = e$, so $\tilde{u}_1 = \tilde{u}_2 = 0$ on sides AB and DC of the unit cell (see Fig. 3). The traction component t_3 is also zero along these sides. The $x_1 - x_2$ plane at $x_3 = 0$ is a plane of anti-symmetry for the component of $\tilde{\mathbf{u}}$ in the direction of x_3 ($\tilde{u}_3$), so $\tilde{u}_3$ is equal to zero on BC. The tractions t_1 and t_2 along this side are also equal to zero. Finally, the fluctuating displacements are anti-symmetric with respect to the midpoint M of the sloping edge of the unit cell and therefore vanish at M. The tractions $\mathbf{t}$ are symmetric with respect to M on the sloping edge.

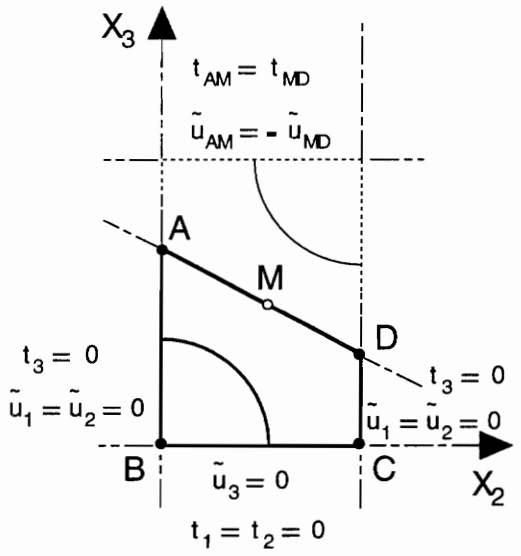

Figure 3. Boundary conditions.

2.4. Finite Element Formulation

As mentioned in Section 1, phenomena such as plastic locking may arise in the plastic range and cause a large overestimation of the equivalent stiffnesses. Before attempting any plastic implementation, it is crucial to test the grid's immunity to locking. We will see later (Section 3) how this can be achieved by simulating constant volume deformations within the elastic range. Therefore, evaluating macroscopic stress-strain relations with the elastic model will constitute an important phase of the model development. This is why the finite element formulation presented in this section is derived for the elastic case only. For the sake of simplicity, thermal loads are also assumed to be zero.

Note that a non-linear incremental finite element formulation can be derived from the principle of virtual work if inelastic phases are assumed. Thermal loads can also be introduced without major modifications. The resulting global elastoplastic load-displacement relations are similar to those obtained for the elastic case (see Ref. 19 and Section 5.2).

Using a displacement formulation, the fluctuating displacement field $\tilde{\mathbf{u}}$ within the n-node element number e is interpolated from the $3n \times 1$ element nodal degrees of freedom (d.o.f.) $\tilde{\mathbf{d}}_e$. With the displacement field decomposition given in Eq. (2), the displacement field within element e, i.e. $\mathbf{u}_e$, can be further rewritten as

$$\mathbf{u}_e = \mathbf{N}_e \tilde{\mathbf{d}}_e + \mathbf{X}\boldsymbol{\epsilon}^o, \tag{4}$$

where $\mathbf{N}_e$ is a $3 \times 3n$ matrix of shape functions for the n-node element number e:

$$\mathbf{N}_e = [\mathbf{I}N_1 \;\; \mathbf{I}N_2 \;\; .... \;\; \mathbf{I}N_n], \tag{5}$$

$\mathbf{I}$ is the 3×3 identity matrix and N_i is the interpolation function at node i for element e.

The strains $\boldsymbol{\epsilon}_e$ are then obtained from the displacements $\mathbf{u}_e$ by differentiation of Eq. (4):

$$\boldsymbol{\epsilon}_e = \mathbf{L}\,\mathbf{N}_e \tilde{\mathbf{d}}_e + \mathbf{I}^* \boldsymbol{\epsilon}^o = \left[\mathbf{B}_e \;\; \mathbf{I}^*\right] \begin{Bmatrix} \tilde{\mathbf{d}}_e \\ \boldsymbol{\epsilon}^o \end{Bmatrix}, \tag{6}$$

where $\mathbf{B}_e = \mathbf{L}\,\mathbf{N}_e$ is the strain-displacement relation matrix, $\mathbf{I}^*$ is a 6×4 selection matrix, which distributes the 4 components of $\boldsymbol{\epsilon}^o$ into the 6 components of $\boldsymbol{\epsilon}$:

$$\mathbf{I}^* = \begin{bmatrix} 0 & 1 & 0 & 0 \\ 0 & 0 & 1 & 0 \\ 1 & 0 & 0 & 0 \\ 0 & 0 & 0 & 0 \\ 0 & 0 & 0 & 0 \\ 0 & 0 & 0 & 1 \end{bmatrix}, \tag{7}$$

and $\mathbf{L}$ is a 6x3 differential operator:

$$\mathbf{L} = \begin{bmatrix} \dfrac{\partial}{\partial x_1} & 0 & 0 \\ 0 & \dfrac{\partial}{\partial x_2} & 0 \\ 0 & 0 & \dfrac{\partial}{\partial x_3} \\ 0 & \dfrac{\partial}{\partial x_3} & \dfrac{\partial}{\partial x_2} \\ \dfrac{\partial}{\partial x_3} & 0 & \dfrac{\partial}{\partial x_1} \\ \dfrac{\partial}{\partial x_2} & \dfrac{\partial}{\partial x_1} & 0 \end{bmatrix}. \tag{8}$$

Following the standard finite element procedure, we express the potential energy Π_p of a cylindrical volume Ω of axis parallel with x_1, the direction of the fiber. This volume has an axial length L as

shown in Fig. 4. Its cross section on the $x_1 = 0$ plane corresponds to the unit cell which has an area of A, and a contour denoted by C. The boundary of Ω which includes the lateral surfaces and the two ends is denoted by Γ.

Assuming elastic phases, no initial strains or stresses, and no body forces or thermal loads, we can write:

$$\Pi_p = \int_{\Omega} \frac{1}{2}\, \boldsymbol{\epsilon}^T \mathbf{E}\, \boldsymbol{\epsilon}\, dV - \int_{\Gamma} \mathbf{t}^T \mathbf{u}\, dS, \tag{9}$$

where $\boldsymbol{\epsilon}$ is the strain field, $\mathbf{E}$ is the material property matrix, $\mathbf{u}$ is the displacement field, and $\mathbf{t}$ are the surface tractions.

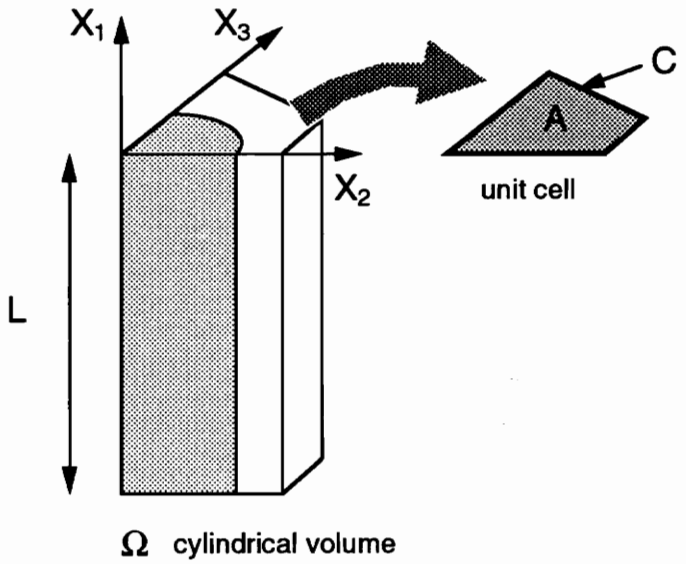

Figure 4. Cylindrical region Ω.

If we decompose Π_p into a sum over the elements e of Ω of volume Ω_e, and substitute the expressions for $\mathbf{u}_e$ and $\boldsymbol{\epsilon}_e$ (Eqs. 4 to 8), we then obtain:

$$\Pi_p = \sum_e \left\{ \int_{\Omega_e} \frac{1}{2} \begin{Bmatrix} \tilde{\mathbf{d}}_e \\ \boldsymbol{\epsilon}^o \end{Bmatrix}^T \begin{bmatrix} \mathbf{B}_e & \mathbf{I}^* \end{bmatrix}^T \mathbf{E}_e \begin{bmatrix} \mathbf{B}_e & \mathbf{I}^* \end{bmatrix} \begin{Bmatrix} \tilde{\mathbf{d}}_e \\ \boldsymbol{\epsilon}^o \end{Bmatrix} d\Omega - \int_{\Gamma_e} \mathbf{t}^T (\mathbf{N}_e \tilde{\mathbf{d}}_e + \mathbf{X}\boldsymbol{\epsilon}^o)\, d\Gamma \right\}. \tag{10}$$

Distributing the matrix products in Eq. (10), we have:

$$\Pi_p = \sum_e \left\{ \int_{\Omega_e} \frac{1}{2} \begin{Bmatrix} \tilde{\mathbf{d}}_e \\ \boldsymbol{\epsilon}^0 \end{Bmatrix}^T \begin{bmatrix} \mathbf{B}_e^T \mathbf{E}_e \mathbf{B}_e & \mathbf{B}_e^T \mathbf{E}_e \mathbf{I}^* \\ \mathbf{I}^{*T} \mathbf{E}_e \mathbf{B}_e & \mathbf{I}^{*T} \mathbf{E}_e \mathbf{I}^* \end{bmatrix} \begin{Bmatrix} \tilde{\mathbf{d}}_e \\ \boldsymbol{\epsilon}^0 \end{Bmatrix} d\Omega - \int_{\Gamma_e} \mathbf{t}^T \mathbf{N}_e \tilde{\mathbf{d}}_e \, d\Gamma - \int_{\Gamma_e} \mathbf{t}^T \mathbf{X} \boldsymbol{\epsilon}^0 \, d\Gamma \right\}. \quad (11)$$

Let us simplify the expression above. The fluctuating displacement field $\tilde{\mathbf{d}}$, and thus the $\mathbf{N}_e$ and $\mathbf{B}_e$ matrices do not depend on the coordinate x_1. Therefore, the volume integrals over elements of Ω in the first term of Eq. (11) can be rewritten in terms of integrals over surface elements A_e of the unit cell multiplied by L, the axial length of Ω.

For the second term, contributions of the integrals over the two ends of Ω cancel out, and the remaining contributions can be rewritten in terms of line integrals over contour elements C_e of the unit cell multiplied by L.

Finally, if we define $\boldsymbol{\sigma}^0$ as the average macro stress field over Ω, we can easily prove, by applying Green's theorem (see Appendix A), that the third term in Eq. (11) reduces to $L A \boldsymbol{\sigma}^0$, where A is the area of the unit cell.

After these transformations, Π_p becomes:

$$\Pi_p = L \sum_e \left\{ \int_{A_e} \frac{1}{2} \begin{Bmatrix} \tilde{\mathbf{d}}_e \\ \boldsymbol{\epsilon}^0 \end{Bmatrix}^T \begin{bmatrix} \mathbf{B}_e^T \mathbf{E}_e \mathbf{B}_e & \mathbf{B}_e^T \mathbf{E}_e \mathbf{I}^* \\ \mathbf{I}^{*T} \mathbf{E}_e \mathbf{B}_e & \mathbf{I}^{*T} \mathbf{E}_e \mathbf{I}^* \end{bmatrix} \begin{Bmatrix} \tilde{\mathbf{d}}_e \\ \boldsymbol{\epsilon}^0 \end{Bmatrix} dA - \int_{C_e} \mathbf{t}^T \mathbf{N}_e \tilde{\mathbf{d}}_e \, dl - A \boldsymbol{\sigma}^0 \boldsymbol{\epsilon}^0 \right\}, \quad (12)$$

which can be rewritten as

$$\frac{\Pi_p}{L} = \frac{1}{2} \begin{Bmatrix} \tilde{\mathbf{d}} \\ \boldsymbol{\epsilon}^0 \end{Bmatrix}^T \begin{bmatrix} \mathbf{K}_1 & \mathbf{K}_2 \\ \mathbf{K}_3 & \mathbf{K}_4 \end{bmatrix} \begin{Bmatrix} \tilde{\mathbf{d}} \\ \boldsymbol{\epsilon}^0 \end{Bmatrix} - \begin{Bmatrix} \mathbf{F} \\ A \boldsymbol{\sigma}^0 \end{Bmatrix}^T \begin{Bmatrix} \tilde{\mathbf{d}} \\ \boldsymbol{\epsilon}^0 \end{Bmatrix}, \quad (13)$$

where $\tilde{\mathbf{d}}$ is the vector of nodal fluctuating displacements,

$$\mathbf{K}_1 = \sum_e \mathbf{K}_{1e} = \sum_e \int_{A_e} \mathbf{B}_e^T \mathbf{E}_e \mathbf{B}_e \, dA, \quad (14)$$

$$\mathbf{K}_2 = \sum_e \mathbf{K}_{2e} = \sum_e \int_{A_e} \mathbf{B}_e^T \mathbf{E}_e \mathbf{I}^* \, dA, \quad (15)$$

$$\mathbf{K}_3 = \sum_e \mathbf{K}_{3e} = \sum_e \int_{A_e} \mathbf{I}^{*T} \mathbf{E}_e \mathbf{B}_e \, dA, \quad (16)$$

$$\mathbf{K}_4 = \sum_e \mathbf{K}_{4e} = \sum_e \int_{A_e} \mathbf{I}^{*T}\, \mathbf{E}_e\, \mathbf{I}^{*}\, dA, \tag{17}$$

and $\mathbf{F}$ is the vector of nodal forces:

$$\mathbf{F} = \sum_e \mathbf{F}_e = \sum_e \int_{C_e} \mathbf{t}^T\, \mathbf{N}_e\, dl. \tag{18}$$

Note that the summation symbols in the above equations indicate that we respectively include the contributions of all elementary stiffness matrices $\mathbf{K}_{ie}$ and elementary load vectors $\mathbf{F}_e$ in the corresponding global stiffness matrix $\mathbf{K}_i$ and the global load vector $\mathbf{F}$.

The minimization of the potential energy per unit length leads to the global load-displacement relation for the unit cell:

$$\begin{bmatrix} \mathbf{K}_1 & \mathbf{K}_2 \\ \mathbf{K}_3 & \mathbf{K}_4 \end{bmatrix} \begin{Bmatrix} \tilde{\mathbf{d}} \\ \boldsymbol{\epsilon}^0 \end{Bmatrix} = \begin{Bmatrix} \mathbf{F} \\ \mathrm{A}\,\boldsymbol{\sigma}^0 \end{Bmatrix}, \tag{19}$$

where $\boldsymbol{\sigma}^0 = \{0,\ \sigma_{11}^0,\ \sigma_{22}^0,\ \sigma_{12}^0\}^T$ is the vector of macroscopic plane stresses associated with the macroscopic strain field $\boldsymbol{\epsilon}^0 = \{\varepsilon_{33}^0,\ \varepsilon_{11}^0,\ \varepsilon_{22}^0,\ 2\varepsilon_{12}^0\}^T$, A is the total area of the unit cell, and $\mathbf{F}$ is the vector of nodal tractions associated with the vector of nodal fluctuating displacements $\tilde{\mathbf{d}}$. $\mathbf{K}_1$ is the stiffness matrix for the fluctuating nodal displacements. $\mathbf{K}_2$ and $\mathbf{K}_3$ are the coupling matrices between fluctuating and macroscopic fields.

On the boundaries of the unit cell other than the sloping edge, the components of $\mathbf{F}$ associated with unspecified components of $\tilde{\mathbf{d}}$ vanish. On the sloping edge, the fluctuating displacement field is antisymmetric and the traction is symmetric about the midpoint M. Therefore, reduction of the numbers of equations and degrees of freedom in Eq. (19) can be performed for each pair of nodes symmetric about M on the sloping edge. Further reduction can be performed for each boundary nodal fluctuating displacement which is specified to be zero. After these reductions, Eq. (19) can be rewritten as

$$\begin{bmatrix} \mathbf{K}'_1 & \mathbf{K}'_2 \\ \mathbf{K}'_3 & \mathbf{K}_4 \end{bmatrix} \begin{Bmatrix} \tilde{\mathbf{d}}' \\ \boldsymbol{\epsilon}^0 \end{Bmatrix} = \begin{Bmatrix} \mathbf{0} \\ \mathrm{A}\,\boldsymbol{\sigma}^0 \end{Bmatrix}, \tag{20}$$

where $\tilde{\mathbf{d}}'$ are the system d.o.f. associated with the fluctuating part of the displacement field.

As mentioned in Section 2.2, at the macroscopic level, the composite is subjected to a plane stress loading $\boldsymbol{\sigma}^0$ in the plane $x_1 - x_2$. The corresponding macrostrain field is $\boldsymbol{\epsilon}^0 = \{\varepsilon_{33}^0,\ \varepsilon_{11}^0,\ \varepsilon_{22}^0,\ 2\varepsilon_{12}^0\}^T$. This model will be used as a tool to perform a strain-controlled simulation in ε_{11}^0, ε_{22}^0, and ε_{12}^0. Therefore, the macrostrain ε_{33}^0 is unknown and constitutes an additional d.o.f. for our system. The

system of Eq. (20) must be repartitioned to include ε_{33}° in the vector of the system d.o.f. Note that this is the reason why the macrostrains had been arranged in an unusual order. The system can be rewritten as:

$$\begin{bmatrix} \mathbf{K}_{w\,w} & \mathbf{K}_{w\,\bar{\varepsilon}} \\ \mathbf{K}_{\bar{\varepsilon}\,w} & \mathbf{K}_{\bar{\varepsilon}\,\bar{\varepsilon}} \end{bmatrix} \begin{Bmatrix} \mathbf{w} \\ \bar{\boldsymbol{\epsilon}} \end{Bmatrix} = \begin{Bmatrix} \mathbf{0} \\ \mathbf{A}\,\bar{\boldsymbol{\sigma}} \end{Bmatrix}, \tag{21}$$

where $\mathbf{w} = \{\, \tilde{\mathbf{d}}'\ \varepsilon_{33}^{\circ} \,\}^{T}$ are the system d.o.f., $\bar{\boldsymbol{\epsilon}} = \{\varepsilon_{11}^{\circ},\ \varepsilon_{22}^{\circ},\ 2\varepsilon_{12}^{\circ}\}^{T}$, and $\bar{\boldsymbol{\sigma}} = \{\sigma_{11}^{\circ},\ \sigma_{22}^{\circ},\ \sigma_{12}^{\circ}\}^{T}$.

3. Evaluation of Mini Model Performance

In the next sections, we introduce our reference model and describe two procedures used to evaluate the performance of the mini model.

3.1. Reference Model

Developed by Hsu [19], this model predicts off-axis elastoplastic characteristics of unidirectional fiber-reinforced composites subjected to a plane stress loading. It uses the unit cell, the superposition method for the displacement, the boundary conditions, and the finite element formulation presented in Section 2.

The 2-D finite element mesh is shown in Fig. 5. It consists of 216 constant-strain triangles and 126 nodes. Three d.o.f. which represent the 3 components of the fluctuating displacement field are allocated at each node. After applying the boundary conditions described in Section 2.3, the number of degrees of freedom reduces to 318.

This dense grid was used to predict several elastoplastic characteristics of a boron/aluminum composite. The stress-strain curves generated were compared to experimental data provided by Becker *et al* [30] and very good agreement was observed. Therefore, this 318 d.o.f. finite element grid will be used as a reference model to evaluate the performance of our mini model.

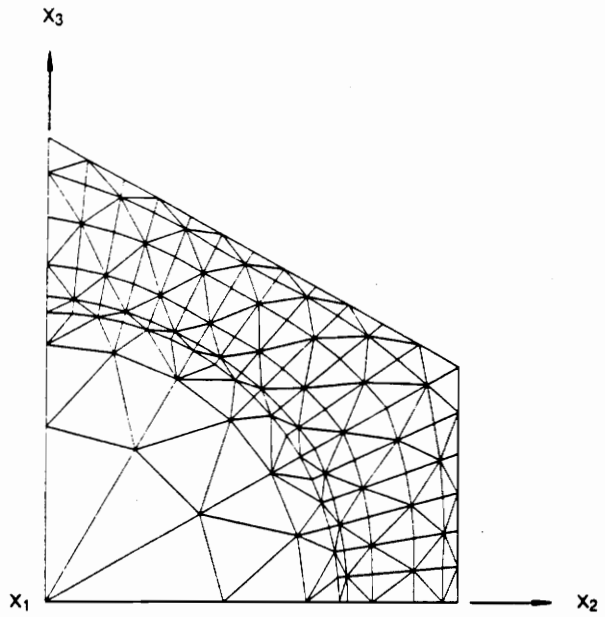

Figure 5. Reference grid.

3.2. Elastic Effective Properties

We recall the global load-displacement relation for the unit cell as derived in Section 2.4:

$$\begin{bmatrix} \mathbf{K}_{w\,w} & \mathbf{K}_{w\,\bar{\varepsilon}} \\ \mathbf{K}_{\bar{\varepsilon}\,w} & \mathbf{K}_{\bar{\varepsilon}\,\bar{\varepsilon}} \end{bmatrix} \begin{Bmatrix} \mathbf{w} \\ \bar{\boldsymbol{\epsilon}} \end{Bmatrix} = \begin{Bmatrix} \mathbf{0} \\ \mathrm{A}\,\bar{\boldsymbol{\sigma}} \end{Bmatrix}, \tag{22}$$

where $\mathbf{w} = \{\tilde{\mathbf{d}}'\ \varepsilon^{\circ}_{33}\}^{\mathrm{T}}$ are the system d.o.f., $\bar{\boldsymbol{\epsilon}} = \{\varepsilon^{\circ}_{11}, \varepsilon^{\circ}_{22}, 2\varepsilon^{\circ}_{12}\}^{\mathrm{T}}$, and $\bar{\boldsymbol{\sigma}} = \{\sigma^{\circ}_{11}, \sigma^{\circ}_{22}, \sigma^{\circ}_{12}\}^{\mathrm{T}}$ are the macroscopic strain and stress fields, respectively, and A is the total area of the unit cell.

In the elastic range, this system is linear. It can be solved for $\bar{\boldsymbol{\sigma}}$ as a function of $\bar{\boldsymbol{\epsilon}}$ simply by eliminating the vector $\mathbf{w}$ of system d.o.f. The effective stress-strain relation for the composite are then obtained as

$$\bar{\boldsymbol{\sigma}} = \mathbf{C}_{\mathrm{c}}\,\bar{\boldsymbol{\epsilon}}, \tag{23}$$

where $\mathbf{C}_{\mathrm{c}}$ is given by

$$\mathbf{C_c} = \frac{-\mathbf{K}_{\bar{\varepsilon}\,w}\,\mathbf{K}_{w\,w}^{-1}\,\mathbf{K}_{w\,\bar{\varepsilon}} + \mathbf{K}_{\bar{\varepsilon}\,\bar{\varepsilon}}}{A}. \tag{24}$$

The matrix $\mathbf{C_c}$ can be identified to the stiffness matrix of an orthotropic material subjected to a plane stress loading in the plane $x_1 - x_2$, and engineering moduli of the composite, E_1, E_2, G_{12}, and ν_{12} can be determined.

These engineering moduli can be computed using the reference grid or the mini model. The comparison between the two predictions will constitute the first evaluation of the performance of the mini model.

3.3. Simulated Plastic Effective Properties

The mini model is intended to predict plastic response of unidirectional fiber-reinforced composites.

A material which deforms plastically encounters large shear deformations in comparison with volumetric change. Therefore, there is a similarity between plastic deformation and elastic deformation of isotropic materials with a large ratio of the bulk modulus K to the shear modulus G. This ratio can be rewritten in terms of the Poisson's ratio ν as $K/G = 2(1 + \nu)/3(1 - 2\nu)$. Note that a large K/G implies ν close to 0.5, which corresponds to an almost incompressible material.

If overly restrictive interpolation functions are used to model displacements, no deformation will be allowed without change in volume and the matrix will not deform at all. This phenomenon is called plastic locking. It is usually avoided by increasing the number of d.o.f. or using reduced integration. In our case, plastic locking could be crucial because of the very small number of d.o.f. Our first concern is then to develop a model immune to this phenomenon.

We can evaluate the performance of the mini model in the plastic range by using an elastic computation with modified material properties for the matrix, (i.e. K/G large). To do this, we simulate the behavior of a composite with a nearly incompressible matrix by adjusting its Poisson's ratio to 0.495 while keeping its bulk modulus constant. The modified Young's modulus is $E = 0.030\,K$. The fiber properties remain unchanged since the fiber is considered linear elastic up to rupture. With these modified phase properties, we can evaluate the engineering moduli for the composite as previously described in Section 3.2 using the mini grid and the reference grid. The comparison between the two predictions will constitute the second evaluation of the performance of the mini model.

4. Mini Grid Development

Our goal is to develop a mini model capable of predicting the same macroscopic strain-stress behavior as the reference grid presented in Section 3.1. The mini model uses the same unit cell, the same superposition method for the displacement field, and the same boundary conditions as the reference model. The two procedures described in Section 3.2 and 3.3 will be used to evaluate the performance of the mini model.

4.1. History of Development

The first mini model we developed used an hexagonal geometry to represent the fiber and contained 3 isoparametric bilinear elements I, II and III as shown in Fig. 6. The hexagonal fiber had the same cross sectional area as a circular fiber of diameter d_f. Three fluctuating displacement d.o.f. were allocated at each node. By applying the boundary conditions described in Section 2.3, the number of d.o.f. reduced to 7 (see arrows in Fig. 6). One more degree of freedom was added to account for the unknown macroscopic strain ε°_{33}.

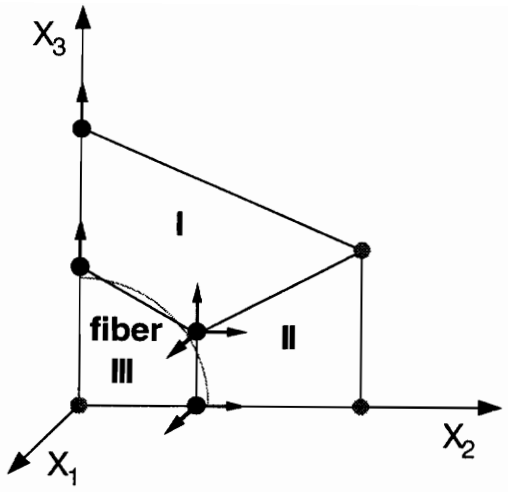

Figure 6. First mini model developed.

To evaluate the performance of this first model, we followed the two procedures described in Section 3. First, this mini model was used to predict effective properties of a boron/aluminum composite in the elastic range. The geometry of the composite is defined by a volume fraction $v_f = 0.460$, a fiber diameter $d_f = 0.142$ mm and a fiber spacing $h = 0.173$ mm as defined in Fig. 2 (from which $e = 0.0995$ mm). This geometry is very close to an hexagonal array. The angle α defined in Fig. 2 is set to 60 degrees. The elastic properties of the fibers and the matrix are: $E_{fiber} = 400$ GPa, $\nu_{fiber} = 0.200$, $E_{matrix} = 72.4$ GPa, and $\nu_{matrix} = 0.330$. The elastic properties predicted by this model were compared to those predicted by the reference model. Good agreement was observed. The largest error was about 3.0% in the prediction of E_2.

Then, in order to test the model's immunity to plastic locking, we performed a plastic simulation on the same geometry as described in Section 3.3. The matrix of the boron/aluminum composite previously analyzed was made almost incompressible by increasing its Poisson's ratio to 0.495 while keeping its bulk modulus unchanged. The change in Poisson's ratio results in a change in the ratio of bulk modulus to shear modulus from 2.60 to 100. The modified Young's modulus is $E_{matrix} = 2.12$ GPa. The effective properties predicted by the mini model were compared to those predicted by the reference model. A discrepancy of 100% on the predictions of E_2 was observed between the two grids; the transverse modulus predicted by the mini model was much higher. This can be attributed to Poisson's ratio locking.

To improve the behavior of the mini grid with respect to locking, we then chose to add more d.o.f. to represent matrix deformations more accurately. Using the reference grid, we computed displacements along the sides of elements I and II of Fig. 6 and compared them to those obtained by linear interpolation of nodal displacements of these elements. The comparison showed that displacements along the sides of element II were far from linear and that a quadratic function would give a much better approximation of the displacement field. Thus, this element was replaced by a quadratic serendipity element and the number of d.o.f. was increased from 8 to 14. We used this second mini model to predict the simulated plastic effective properties of the same boron/aluminum composite. The predictions of this new model were compared once again with predictions of the reference model. Discrepancies of up to 80% were still observed between the two sets of results. The transverse modulus predicted by the mini grid was still much higher than that predicted by the reference grid.

This discrepancy indicated that another factor besides the number of d.o.f. used to represent the matrix deformations caused this discrepancy. We speculated that the large difference in effective properties between the mini model and the reference grid might be due to a difference in fiber geometry. The reference model uses a circular geometry to represent the fiber, while the mini model used a simplified hexagonal geometry. In order to compare these two geometries, simulated plastic effective properties of the same boron/aluminum composite were computed with two different fine grids, one using hexagonal fibers and the other circular fibers (reference grid). The cross sectional area of the fiber was the same for both grids. The transverse modulus was 48% higher for the hexagonal fiber cross section than for the circular fiber cross section (see Table 1). This difference indicates that internal geometry affects the properties of the composite in the plastic range. Therefore, our next effort was to develop a mini model using the more realistic circular geometry to represent the fibers. This model is presented in the next section.

Table 1. Simulated plastic effective material properties for boron/al. composite using different geometries for the fibers. Refer to Fig. 2 for the unit cell axis system.

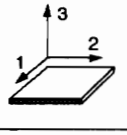	Fine Grid 	Fine Grid 
E_1 (GPa)	185.0	185.2
E_2 (GPa)	8.669	12.84
G_{12} (GPa)	1.906	1.953
ν_{12}	0.3589	0.3587

v_f = 46.00%, E_f = 400.0 GPa, ν_f = 0.2000, E_m = 2.122 GPa, ν_m = 0.4950

4.2. Finite Element Discretization

We now describe in details a mini grid with a circular cross section fiber element.

The mini grid is shown in Fig. 7; it uses 4 elements. Elements I, II, and III discretize the matrix, while element IV represents the fiber.

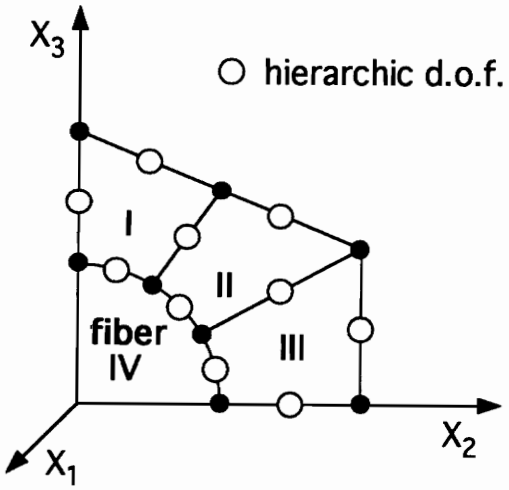

Figure 7. Mini grid.

4.2.1. Fluctuating Displacement Field

4.2.1.1. Matrix

The matrix is divided into 3 hierarchic [31] elements I, II and III as shown in Fig. 7. Hierarchic elements are isoparametric bilinear elements with quadratic corrections added along the sides. The resulting elements are either subparametric or isoparametric (distorted elements). The degrees of freedom associated with the quadratic hierarchic shape functions measure the departure from linearity at the midpoint along each side of the element.

Examples of simple, 1-D linear elements with standard shape functions and with quadratic hierarchic shape functions are shown in Fig. 8.

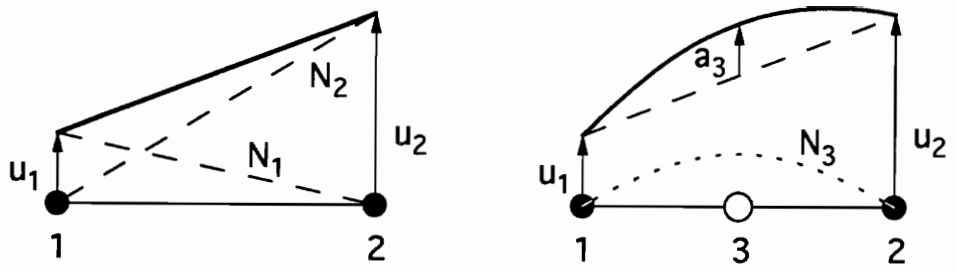

Figure 8. Linear elements with standard and hierarchic shape functions.

For the linear element with standard shape functions, the displacement field $u = N_1u_1 + N_2u_2$ is linear, while the displacement field for the linear element with quadratic hierarchic shape function $u = N_1u_1 + N_2u_2 + N_3a_3$ is quadratic. The degree of freedom a_3 measures the amplitude of the quadratic correction, i.e. the magnitude of the departure from linearity of the displacement approximation at the element center since the shape function N_3 is equal to one at that point and vanishes at the end points.

Our first concern was to develop a mini model immune to plastic locking; this is the reason why quadratic corrections were added along every side of the elements discretizing the matrix. However, minimizing the number of d.o.f. is also desirable. We will see in Section 4.4 that not all these quadratic corrections are needed to prevent plastic locking and linear displacement approximations in some directions are sufficient along some sides of the elements representing the matrix. Note that the use of hierarchic shape functions instead of regular serendipity shape functions allows us to switch from quadratic to linear approximation in a particular direction by simply setting the associated quadratic correction to zero. For this reason, the use of "hierarchic elements" proved very valuable in the process of minimizing the number of d.o.f. in our model.

The 2-D hierarchic interpolations functions used for the mini model are given in Appendix B. Note that displacement compatibility along element interfaces for 2-D "quadratic hierachic elements" is guaranteed when the quadratic correction is shared. The nodes are numbered as indicated in Fig. 9. Regular d.o.f. are represented by bullets, while hierarchic d.o.f. are represented by circles. Both are associated with the fluctuating displacement field.

The coordinates of nodes 4, 9, 13 and 19 are expressed in terms of the 3 parameters d_f, e and h introduced in Section 2.1. Node 4 of coordinates (e/2,h/2) is at the midpoint along the sloping edge. The sloping edge, and thus nodes 1 and 21, are completely determined by the angle α which can take any value as long as the edge lies entirely in the matrix phase. We arbitrarily set this angle to 60 degrees. The fiber boundary is a quarter of circle (radius $d_f/2$) and nodes 13 to 19 are located on that boundary. Nodes 15 and 17 are respectively defined as the intersection between the fiber

boundary and lines from the origin of the coordinate system to nodes 4 and 21. Finally, all d.o.f. with quadratic corrections are measured at the midpoints along hierarchic element sides.

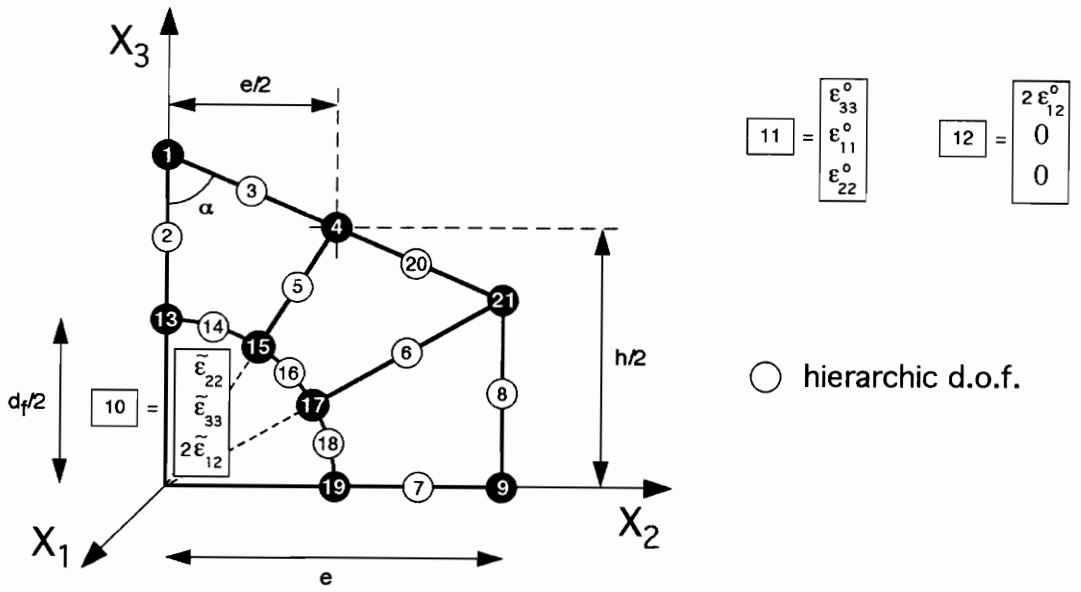

Figure 9. Geometry of the mini grid.

4.2.1.2. Fiber

The fiber is represented by element IV of Fig. 7, which has a circular geometry. The strain field associated with the fluctuating part of the displacement field inside the fiber, $\tilde{\boldsymbol{\epsilon}}_{IV} = \{\tilde{\varepsilon}_{11}, \tilde{\varepsilon}_{22}, \tilde{\varepsilon}_{33}, 2\tilde{\varepsilon}_{23}, 2\tilde{\varepsilon}_{13}, 2\tilde{\varepsilon}_{12}\}^T$ is assumed to be uniform. The boundary conditions described in Section 2.3 along the sides $x_2 = 0$ and $x_3 = 0$ of the fiber lead to $\tilde{\varepsilon}_{13} = \tilde{\varepsilon}_{23} = 0$. Also, $\tilde{\varepsilon}_{11}$ is equal to zero since the fluctuating displacement field does not depend on x_1. Thus the fluctuating strain field inside the fiber reduces to

$$\tilde{\boldsymbol{\epsilon}}_{IV} = \{0, \tilde{\varepsilon}_{22}, \tilde{\varepsilon}_{33}, 0, 0, 2\tilde{\varepsilon}_{12}\}^T. \tag{25}$$

The remaining non zero components, (i.e. $\tilde{\varepsilon}_{22}$, $\tilde{\varepsilon}_{33}$, and $2\tilde{\varepsilon}_{12}$), can be used as d.o.f. for the fiber. These 3 d.o.f. are grouped into a fictitious node 10 (see Fig. 9). The resulting fluctuating displacement field $\tilde{\mathbf{u}}_{IV}$ inside the fiber is a linear function of x_2 and x_3 and is written as

$$\tilde{\mathbf{u}}_{IV} = \begin{bmatrix} 0 & 0 & x_2 \\ x_2 & 0 & 0 \\ 0 & x_3 & 0 \end{bmatrix} \begin{Bmatrix} \tilde{\varepsilon}_{22} \\ \tilde{\varepsilon}_{33} \\ 2\tilde{\varepsilon}_{12} \end{Bmatrix} = \mathbf{N}_{IV} \begin{Bmatrix} \tilde{\varepsilon}_{22} \\ \tilde{\varepsilon}_{33} \\ 2\tilde{\varepsilon}_{12} \end{Bmatrix}. \tag{26}$$

4.2.2. Macrostrain Field

For programming convenience, two fictitious nodes, number 11 and 12 (see Fig. 9), are created to contain the macroscopic strain field $\epsilon^o = \{\varepsilon^o_{33}, \varepsilon^o_{11}, \varepsilon^o_{22}, 2\varepsilon^o_{12}\}^T$. The macrostrains ε^o_{33}, ε^o_{11}, and ε^o_{22} are allotted to node 11, while $2\varepsilon^o_{12}$ is allotted to node 12.

4.2.3. Number of degrees of freedom

After imposing the boundary conditions and the fluctuating displacement continuity conditions, the number of d.o.f. associated with the fluctuating part of the displacement field reduces to 17. One extra d.o.f. must be added to account for the unknown macroscopic strain ε^o_{33}. The remaining d.o.f. are shown in Fig. 10 and include: 1 regular d.o.f. represented by a bullet, 13 hierarchic d.o.f. represented by circles, 3 fluctuating strains in the fiber and the macrostrain ε^o_{33}.

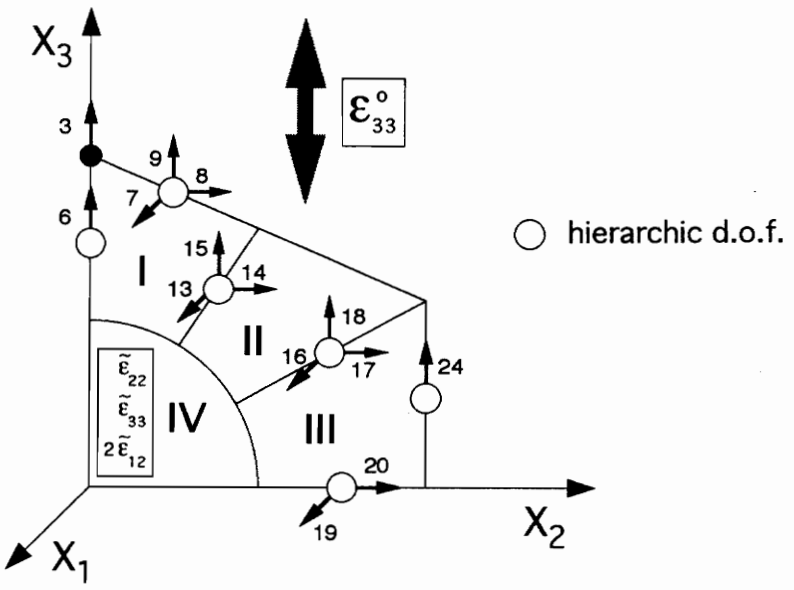

Figure 10. Degrees of freedom of the mini grid (18 d.o.f.).

Note that in the plastic range, the material properties of the matrix will change as a function of the strain (the fiber is assumed linear elastic to rupture). Computation of the elementary stiffnesses of the elements discretizing the matrix and imposition of the boundary conditions will have to be repeated in an iterative solution procedure. In order to reduce computational time, the strain-displacement relation matrices (or **B** matrices) defined in Eq. (6) of Section 2.4 are computed for each element (see Appendix B), and then modified to account for the boundary conditions and the

fluctuating displacement continuity conditions. These computations can be performed beforehand in a preprocessor unit, saving computational time.

4.3. Mini Grid Performance

In this section, we evaluate the performance of the mini grid introduced in Section 4.2 using the two procedures presented in Section 3.

Our mini model is used to predict elastic effective properties and simulated plastic effective properties of the boron/aluminum composite described in Section 4.1. We recall its characteristics. The geometry of the composite is defined by a volume fraction $v_f = 0.460$, a fiber diameter $d_f = 0.142$ mm and a fiber spacing $h = 0.173$ mm as defined in Fig. 2 of Section 2.1 (from which $e = 0.0995$ mm). This geometry is very close to an hexagonal array. The angle α defined in Fig. 2 is set to 60.0 degrees. The elastic properties of the fibers and the matrix are: $E_{fiber} = 400$ GPa, $\nu_{fiber} = 0.200$, $E_{matrix} = 72.4$ GPa, and $\nu_{matrix} = 0.330$.

4.3.1. Elastic Range

Effective properties in the elastic range are examined first. The effective properties predicted by the mini grid are given in Table 2 and are compared to those predicted by the reference model. Very good agreement is observed. The largest error is about 0.4% in the value of E_2.

Table 2. Elastic effective material properties for boron/al. composite. Refer to Fig. 2 for the unit cell axis system.

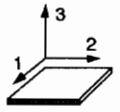	Fine Grid 318 d.o.f	Mini Grid 18 d.o.f
E_1 (GPa)	223.3	223.5
E_2 (GPa)	140.0	140.5
G_{12} (GPa)	54.19	54.19
ν_{12}	0.2637	0.2637

$v_f = 46.00\%, E_f = 400.0$ GPa, $\nu_f = 0.2000, E_m = 72.40$ GPa, $\nu_m = 0.3300$

4.3.2. Simulated Plastic Range

The next test primarily addresses the immunity of the mini grid to plastic locking. As explained in Section 3.3, this is achieved through a "plastic" simulation. It consists of an elastic calculation on a composite with quasi incompressible matrix. Starting with the elastic properties listed above, the matrix is made almost incompressible by increasing its Poisson's ratio to $\nu_{matrix} = 0.495$, while keeping its bulk modulus unchanged. The modified Young's modulus is $E_{matrix} = 2.12$ GPa, while the modified ratio of the bulk modulus to the shear modulus equal to 100. The geometry of the array and the fiber properties are as in Section 4.3.1. The simulated plastic effective properties predicted by the mini model are computed using a 2 by 2 Gauss rule for elements I, II and III of Fig. 10 and are compared once again with predictions of the reference model (see Table 3). Very good agreement is observed. The largest error is about 3% in the value of E_2. These results indicate that locking has been avoided despite the very small number of d.o.f.

Note that the ratio of the bulk modulus to the shear modulus which is characteristic of inelastic deformation of usual matrix materials is typically lower than 100, so that our mini model should be immune to locking in most practical cases.

Table 3. Simulated plastic effective material properties for boron/al. composite. Refer to Fig. 2 for the unit cell axis system.

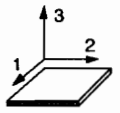	Fine Grid 318 d.o.f	Mini Grid 18 d.o.f
E_1 (GPa)	185.5	185.2
E_2 (GPa)	8.669	8.929
G_{12} (GPa)	1.906	1.904
ν_{12}	0.3589	0.3585

$v_f = 46.00\%, E_f = 400.0$ GPa, $\nu_f = 0.2000, E_m = 2.122$ GPa, $\nu_m = 0.4950$

4.4. Further Minimization of Mini Grid Size

Performing a plastic analysis of a composite can be very costly, and even a small reduction of d.o.f. can be significant in minimizing computational cost. This can be achieved by removing one by one the d.o.f. which is least needed to model the fluctuating displacements (i.e. produces the smallest

deterioration in simulated plastic effective properties when removed from the model). The algorithm is described in Fig. 11; it starts with the 18 d.o.f. model of Section 4.2 and removes d.o.f. while keeping modeling errors within a predefined range.

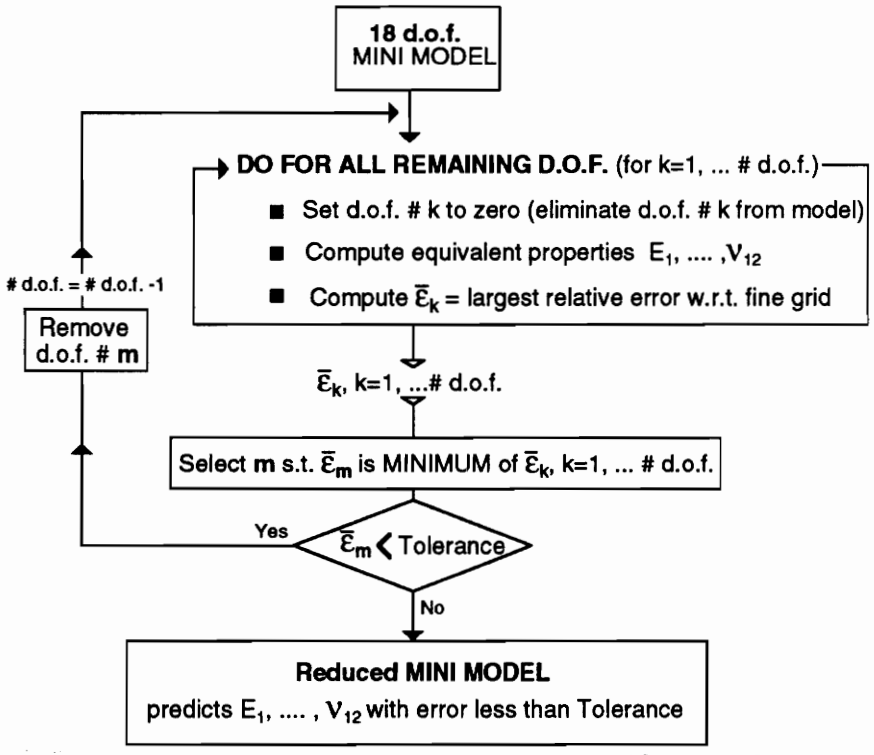

Figure 11. Optimization process.

As an illustration, the number of d.o.f. for a boron/aluminum composite with the characteristics defined in Section 4.3 can be reduced from 18 to 12 if a tolerance of 8% on the effective properties is chosen. During the first stage of the optimization process, when going from 18 to 14 d.o.f., the errors tend to become evenly distributed among the effective properties. All quadratic corrections in the x_1 direction (number 7, 13, 16 and 19 in Fig. 10) are removed during this phase and decrease the accuracy of G_{12}, while the errors on other engineering moduli remain essentially unaffected. Then, when the number of d.o.f. is further reduced from 14 to 11, the quadratic corrections 6, 14 and 9 (see Fig. 10) are successively eliminated and the error on E_2 increases up to 9.3% while the error on G_{12} remains unchanged. The evolution of the relative errors on E_2 and G_{12} during the optimization is shown in Fig. 12. In comparison to typical errors introduced by existing plasticity models, an error of 5% seems acceptable and the 12 d.o.f. mini model will be used for future elastoplastic analyses.

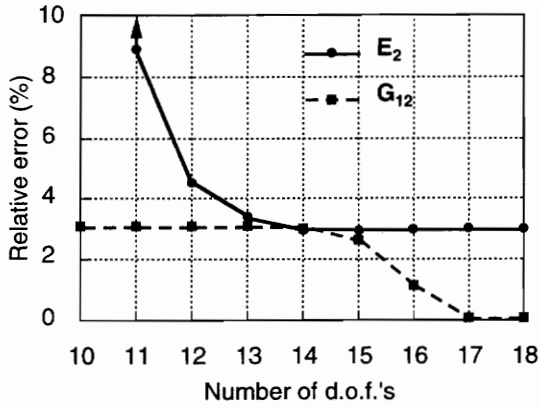

Figure 12. Relative errors on simulated plastic effective properties versus the number of d.o.f. for boron/al.

The effective properties computed by the 14 and the 12 d.o.f. models are given in Table 4. The maximum error with respect to fine grid are about 3.1% on G_{12} for the model containing 14 d.o.f. and 4.6% on E_2 for the 12 d.o.f. model.

Table 4. Simulated plastic effective material properties for boron/al. composite predicted by reduced mini grids. Refer to Fig. 2 for the unit cell axis system.

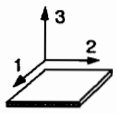	Fine Grid 318 d.o.f	Mini Grid 14 d.o.f	Mini Grid 12 d.o.f
E_1 (GPa)	185.0	185.2	185.2
E_2 (GPa)	8.669	8.929	9.062
G_{12} (GPa)	1.906	1.965	1.965
ν_{12}	0.3589	0.3585	0.3606

$v_f = 46.00\%, E_f = 400.0$ GPa, $\nu_f = 0.2000, E_m = 2.122$ GPa, $\nu_m = 0.4950$

Note however that the optimal reduction of d.o.f. depends on the nature of the composite (both its geometry and the properties of its constituents). Therefore, this simple optimization process could be performed for each composite system before attempting any macro-micro integrated analysis.

5. Plastic Implementation

A mini model involving very few d.o.f. (18) has been presented. It is capable of predicting effective elastic properties of unidirectional fiber-reinforced composites under plane stress loading with excellent accuracy (0.4%). Its immunity to plastic locking was demonstrated by obtaining effective properties with incompressible matrix material. Its number of d.o.f. can be further reduced by a simple optimization process. In view of these results, good behavior in the plastic range can be expected. For this, we need to incorporate a plastic model of the matrix phase (the fibers are assumed linear elastic).

The first section of this chapter briefly summarizes the particular elastoplastic model used in this study. Then, the iterative procedure used to solve the non-linear strain-controlled equilibrium equations is presented.

5.1. Matrix Plasticity Model

In order to make a fair comparison, the plasticity model for the matrix is the same as the one used in the reference model. The plastic behavior of the matrix is modeled with the endochronic constitutive theory without a yield surface.

First introduced by Valanis [32], this theory is based on the laws of irreversible thermodynamics and provides a unified approach for describing the behavior of materials in both the elastic and the plastic range. A few observations can help us understand the basic concepts of this plasticity theory. It is known that materials such as metals exhibit non-linear response even in the very early stages of deformations. Therefore, it can be difficult in some cases to define an elastic limit. The

endochronic theory avoids this difficulty since it does not involve the notion of yield surface. It is also known that the plastic behavior of a material is function of its "history" of strains, stresses and changes in temperature. We can think of this history in terms of an intrinsic "time" which is a property of the material and should give a measure of the plastic state of the material. Based on these observations, the endochronic plasticity theory enforces that the state of stress at a material point, at an "instant" z in the intrinsic "time" scale, is a functional of the entire history of deformation of the material point with respect to the intrinsic time. For any value z of this intrinsic time, the state of stress is written as

$$\sigma_{ij}(z) = \int_0^z C_{ijkl}(z - z') \frac{d\varepsilon_{kl}^p}{dz'} dz', \tag{27}$$

where σ_{ij} is the stress tensor, ε_{kl}^p is the plastic strain tensor representing the amount of deformation deviating from the initial linearity, the kernel C_{ijkl} is a fourth order tensor, and z' is the independent variable of integration, going from 0 to z.

For isotropic materials, the stress tensor can be recast into its hydrostatic and deviatoric parts. If plastic incompressibility is further assumed, the hydrostatic stress response is directly related to the **elastic** volumetric change and only the deviatoric portion of the stress tensor (s_{ij}) needs to be considered. With these hypotheses, the endochronic constitutive equation is rewritten as follows:

$$s_{ij} = \int_0^z \rho(z - z') \frac{d\varepsilon_{ij}^p}{dz'} dz', \tag{28}$$

where $\rho(z)$ is a scalar material function and is referred to as the hereditary function.

It has been shown [33] that the most appropriate measure of the intrinsic time step for rate-independent non-hardening isotropic materials is given by a scaled norm of the plastic strain tensor:

$$dz = (d\varepsilon_{ij}^p d\varepsilon_{ij}^p)^{1/2}. \tag{29}$$

If no yield surface is considered, it has been shown [34] that the function $\rho(z)$ may be approximated with an n-term Dirichlet series,

$$\rho(z) = \sum_{r=1}^{n} C_r e^{-\alpha_r z}. \tag{30}$$

This function should also satisfy a number of requirements [34]: $\rho(0)$ should be sufficiently large in order to insure instantaneous elastic response at initial loading and loading reversals, and C_r and

α_r should be such that $\alpha_1 = 0$, $C_1 \geq 0$, and α_r and C_r are positive for $r \geq 2$. This last set of parameters C_r, and α_r are material constants which govern the elastoplastic behavior and have to be determined experimentally.

The numerical integration of the endochronic constitutive equation (Eq. 28) has been extensively discussed by Hsu [19] and is based on a piecewise linearization of the plastic strain path. By taking into account the hydrostatic (elastic) part of the stress tensor, we can establish a differential stress-strain relation. The tangent stiffness matrix used in the iterative technique to solve the non-linear strain-controlled equilibrium equations can be further derived. For more details regarding these procedures, the reader is referred to Appendix C and reference [19].

5.2. Strain-Controlled Plastic Implementation

Our goal is to predict elastoplastic stress-strain characteristics of our composite model. Within the plastic range, material response is path-dependent, and both macroscopic strain and stress fields have to be discretized into increments. For example, let us say that our system is at a state of co-ordinates ($\bar{\boldsymbol{\epsilon}}, \bar{\boldsymbol{\sigma}}$) in the macroscopic strain-stress space. We want to apply a macrostrain increment $\Delta\bar{\boldsymbol{\epsilon}} = \{\Delta\varepsilon^{\circ}_{11}, \Delta\varepsilon^{\circ}_{22}, 2\Delta\varepsilon^{\circ}_{12}\}^{T}$. Our composite system will then move to a state ($\bar{\boldsymbol{\epsilon}} + \Delta\bar{\boldsymbol{\epsilon}}, \bar{\boldsymbol{\sigma}} + \Delta\bar{\boldsymbol{\sigma}}$).

If inelastic phases are assumed, a non-linear incremental global load-displacement relation for the unit cell, similar to that previously introduced in Eq. (21) of Section 2.4, can be derived from the principle of virtual work. This relation is non-linear with respect to the increments of macrostrains and fluctuating displacements because of matrix plasticity. To solve it, we use a modified Newton-Raphson technique.

For the first iteration, this global load-displacement relation is given by

$$\begin{bmatrix} \mathbf{K}_{w\,w} & \mathbf{K}_{w\,\bar{\varepsilon}} \\ \mathbf{K}_{\bar{\varepsilon}\,w} & \mathbf{K}_{\bar{\varepsilon}\,\bar{\varepsilon}} \end{bmatrix} \begin{Bmatrix} \Delta \mathbf{w}_1 \\ \Delta\bar{\boldsymbol{\epsilon}} \end{Bmatrix} = \begin{Bmatrix} \mathbf{0} \\ \mathrm{A}\,\Delta\bar{\boldsymbol{\sigma}} \end{Bmatrix}, \tag{31}$$

where the matrices $\mathbf{K}_{w\,w}$, $\mathbf{K}_{w\,\tilde{\imath}}$, $\mathbf{K}_{\tilde{\imath}\,w}$, and $\mathbf{K}_{\tilde{\imath}\,\tilde{\imath}}$ are based on the elastic stiffnesses, $\Delta\mathbf{w}_1$ corresponds to the first fluctuating displacement increment and A is the surface of the unit cell. The system defined above is decoupled and only the first equation, needs to be solved for $\Delta\mathbf{w}_1$, i.e.:

$$\mathbf{K}_{w\,w}\ \Delta\mathbf{w}_1 + \mathbf{K}_{w\,\bar{\varepsilon}}\ \Delta\bar{\boldsymbol{\epsilon}} = 0. \tag{32}$$

Next, for all subsequent ith iterations, a new $(\mathbf{K}_{ww})_i$ is constructed. The internal equilibrium is not satisfied and a correction in Δw, i.e. $\delta(\Delta w)_i$ which corresponds to a load imbalance $\delta \mathbf{F}_i$ can be computed as

$$(\mathbf{K}_{w\,w})_i\, \delta(\Delta w)_i = \delta \mathbf{F}_i. \tag{33}$$

This residual force corresponds to the difference between the force due to applied loading and the one due to internal stress. The vector Δw is then updated as

$$\Delta w_{i+1} = \Delta w_i + \delta(\Delta w)_i. \tag{34}$$

This procedure is repeated until the magnitude of the adjustement in Δw, $\delta(\Delta w)_i$ is negligible with respect to $(\Delta w)_i$.

Note that in order to reduce computational time, the matrix $\mathbf{K}_{ww}$ is not updated at every iteration. When $\mathbf{K}_{ww}$ is not updated, we have a constant stiffness iteration, otherwise we have a a Newton-Raphson iteration. The strategy used to choose the type of iteration is described in detail in [19].

Once convergence has been reached, the unknown macrostress increment $\Delta\overline{\sigma}$ is obtained simply by dividing by A the global force vector corresponding to the second equation of the system (31).

Note that if thermal loads are applied, the non-linear incremental global load-displacement relation for the first iteration becomes

$$\begin{bmatrix} \mathbf{K}_{w\,w} & \mathbf{K}_{w\,\bar{\varepsilon}} \\ \mathbf{K}_{\bar{\varepsilon}\,w} & \mathbf{K}_{\bar{\varepsilon}\,\bar{\varepsilon}} \end{bmatrix} \begin{Bmatrix} \Delta w_1 \\ \Delta\overline{\epsilon} \end{Bmatrix} = \begin{Bmatrix} \Delta \mathbf{F}^t \\ A\,\Delta\overline{\sigma} \end{Bmatrix}, \tag{35}$$

where $\Delta \mathbf{F}^t$ is the global force vector due to an increment of internal thermostrains. In this case, the procedure described above remains unchanged except for Eq. (32) which needs to be solved initially with a non zero right-hand side.

6. Application: Elastoplastic response of a Boron/Aluminum Composite

The mini model is used to predict various elastoplastic responses of a boron/aluminum composite. We compare the predictions of the mini model to those of the reference model. For off-axis tensile tests, experimental data published by Becker *et al* [30] are also shown.

The parameters defining the geometry of the composite array are estimated from micrograph of a boron/aluminum composite given in [30].

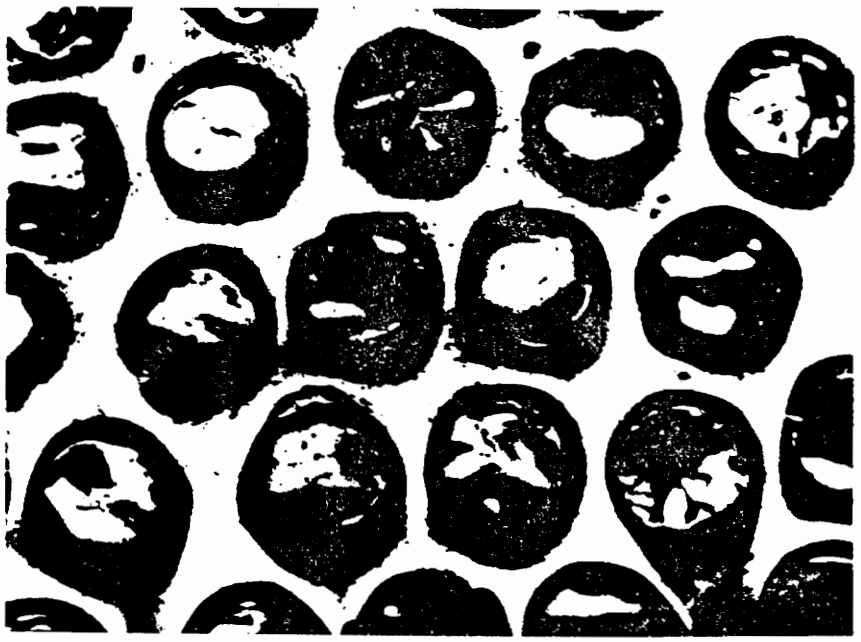

Figure 13. Micrograph of a boron/aluminum composite (135 X).

The geometry of the composite is defined by a volume fraction $v_f = 0.460$, a fiber diameter $d_f = 0.142$ mm and a fiber spacing $h = 0.173$ mm as defined in Fig. 2 of Section 2.1 (from which $e = 0.0995$ mm). This geometry is very close to an hexagonal array. The boron fibers are assumed elastic and isotropic, with a Young's modulus of $E_{fiber} = 400$ GPa, and a Poisson's ratio of $\nu_{fiber} = 0.200$. The aluminum matrix is also assumed isotropic. Its elastic properties are $E_{matrix} = 72.4$ GPa, and $\nu_{matrix} = 0.330$. The thermal expansion of both phases is also assumed isotropic. The coefficient of thermal expansion of the fibers is $\beta_{fiber} = 2.80 \times 10^{-6}\ (°F)^{-1}$, while the coefficient of thermal expansion of the matrix is $\beta_{matrix} = 13.0 \times 10^{-6}\ (°F)^{-1}$.

The plastic behavior of the matrix is modeled using the endochronic theory without a yield surface. The kernel $\rho(z)$ is represented by a four-term Dirichlet series (Eq. 30, Section 5.1) with $C_1 = 0.843$ GPa, $\alpha_1 = 0$, $C_2 = 5.12$ GPa, $\alpha_2 = 3.20 \times 10^2$, $C_3 = 80.0$ GPa, $\alpha_3 = 3.60 \times 10^3$, $C_4 = 178 \times 10^2$ GPa, and $\alpha_4 = 4.00 \times 10^5$. The parameters α_r, $r = 1, 2, 3, 4$, are classical endochronic parameters for the regular 6061-O aluminum alloy, while the parameters C_r, $r = 1, 2, 3, 4$, are essentially determined by curve fitting the stress-strain curve from an axial test on a 10° specimen (see ref. [19] for more details). The intrinsic time z is initially equal to zero at each material point of the matrix.

6.1. Pure Transverse Tensile Response

In this section, we simulate the pure transverse tensile response of the boron/aluminum composite described above ($\varepsilon^\circ_{11} = 0$, $2\varepsilon^\circ_{12} = 0$, $\varepsilon^\circ_{22} = 0.8\%$). Our goal is to compare the prediction of the mini model to the prediction of the reference model.

Predictions of the transverse stress-strain behavior from the 18 degrees of freedom (d.o.f.) (Section 4.2) and 12 d.o.f. (Section 4.4) mini grids are plotted in Fig. 14 and compared to the predictions of the reference grid. The continuous line represents the prediction of the reference model. The prediction of the 12 d.o.f. mini grid is represented by the broken line, while the broken line with triangles represent the prediction of the 18 d.o.f. mini grid. This simulation is performed in 20 steps.

The predictions of the mini grid are above (stiffer than) those of the reference model because of the small number of d.o.f. There is essentially no difference between the predictions of the 18 and 12 d.o.f. models. This was expected since there is only 1% difference on E_2 in the simulated plastic range between the two mini grids (see Section 4.4). Very good agreement is observed between the

reference model and the mini grids. There is no significant discrepancy up to $\varepsilon_{22} = 0.5\%$, which usually is the maximum strain of practical interest.

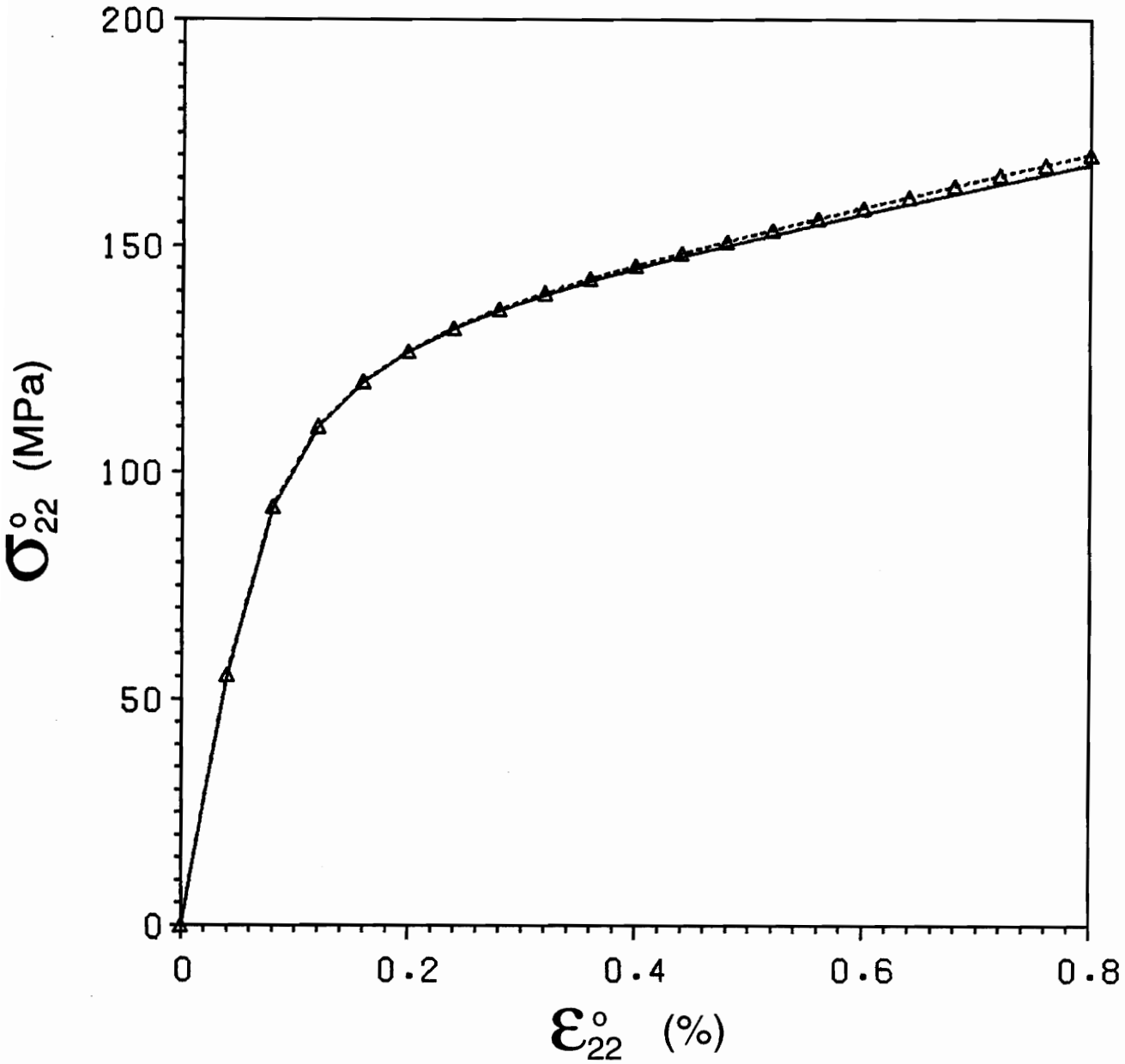

Figure 14. Pure transverse tensile response of boron/aluminum: The broken line shows the response of the 12 d.o.f. mini grid, while the broken line with triangles shows the response of the 18 d.o.f. grid. The continuous line represents the prediction of the reference model.

6.2. *Pure Shear Response*

In this section, we simulate the pure shear response of the same boron/aluminum composite ($\varepsilon_{11}^{o} = 0, \varepsilon_{22}^{o} = 0, 2\varepsilon_{12}^{o} = 0.8\%$ in 20 steps). Our goal is to compare once again the prediction of the mini model to the prediction of the reference model.

Predictions of the shear stress-strain behavior from the 18 d.o.f. (Section 4.2) and 12 d.o.f. (Section 4.4) mini grids are plotted in Fig. 15 and compared to the predictions of the reference grid. The continuous line represents the prediction of the reference model. The prediction of the 12 d.o.f. mini grid is represented by the broken line, while the broken line with triangles represent the prediction of the 18 d.o.f. mini grid.

The prediction of the 18 d.o.f. mini grid exactly matches that of the reference grid. As a matter of fact, there is no difference on G_{12} in the simulated plastic range between these two grids (see Section 4.3). The 12 d.o.f. mini grid prediction shows a discrepancy of about 3% as expected from the simulated plastic properties given in Section 4.4, which is still satisfactory.

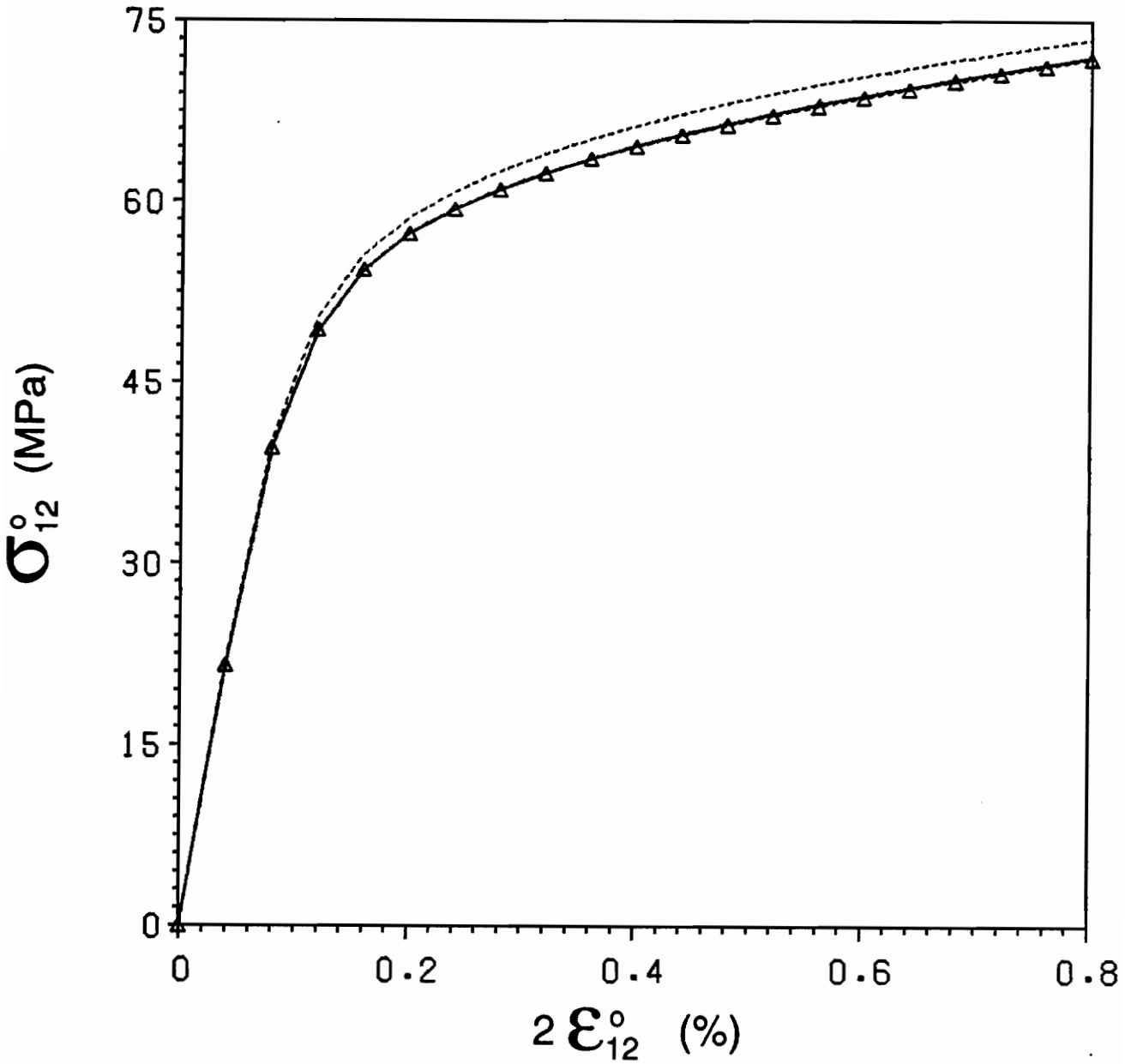

Figure 15. Pure shear response of boron/aluminum: The broken line shows the response of the 12 d.o.f. mini grid, while the broken line with triangles shows the response of the 18 d.o.f. grid. The continuous line represents the prediction of the reference model.

6.3. *Off-Axis Responses*

As evidenced in the pure transverse and shear response predictions presented in the last two sections, the 12 d.o.f. mini model appears to give satisfactory results and is therefore used in this section to predict off-axis responses of the boron/aluminum composite previously described. Our goal is to compare the predictions of the 12 d.o.f. mini grid to thoses of the reference grid. In addition, we show experimental data reported by Becker *et al* [30]. Agreement between the predictions from the reference grid and experimental data has been discussed in [19], and in general, good agreement was found. Therefore, we concentrate here on the agreement between the predictions of the mini grid and the reference model.

A cool-down of $-$ 10°F is applied before the beginning of each tensile test. All simulations are performed in 21 steps. Tensile curves are shown in Figs. 16 to 29 for 0°, 10°, 15°, 30°, 45°, 60°, and 90° specimens. On these figures, the experimental responses are represented by the squares, the broken lines represent the prediction of the mini model, while the continuous lines represent the prediction of the reference model. Note that at the end of the cool-down, the normal macrostrains are negative because of the thermal contraction of the fibers and the matrix. In the figures, the macrostrains are offset so that they read zero at the beginning of the **mechanical** loading.

The response of the 0° specimen is almost linear since the tension is applied in the direction of the fibers, and the mini grid prediction exactly matches that of the reference model. For low fiber angles (10° and 15° specimens) or the highest fiber angle (90° specimen), either shear non-linearity or transverse non-linearity of the matrix dominates. For these fiber angles, no difference between the mini grid prediction and the reference grid prediction is observed. For higher fiber angles, i.e. for the 30°, 45°, and 60° specimens, shear non-linearity and transverse non-linearity of the matrix add together. In this case, a slight discrepancy between the two predictions can be noticed; nevertheless the agreement is generally considered good.

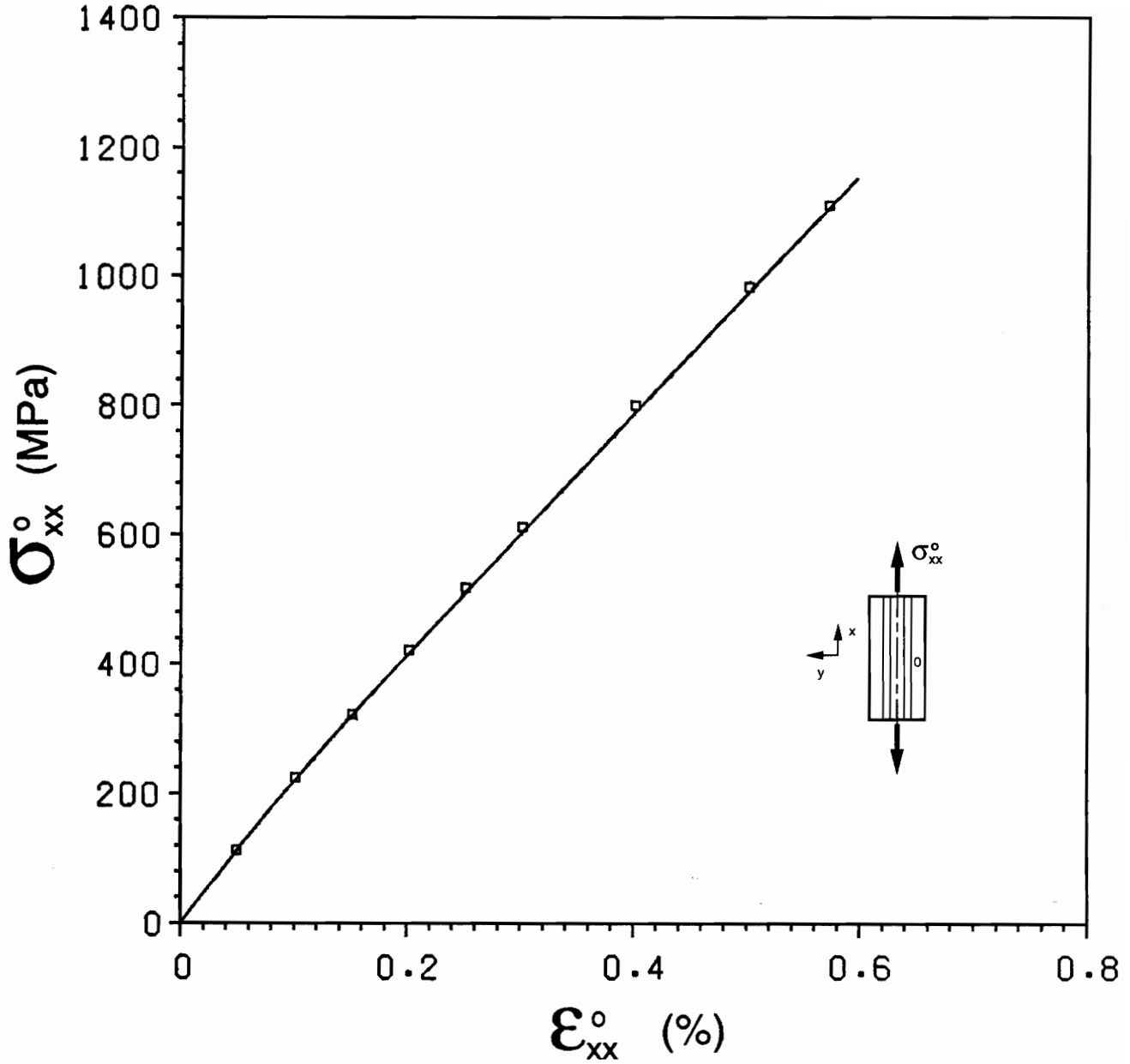

Figure 16. Axial response of 0° specimen: The broken line represents the prediction of the 12 d.o.f. mini grid, while the continuous line represents the prediction of the reference model. The squares correspond to experimental data from [30].

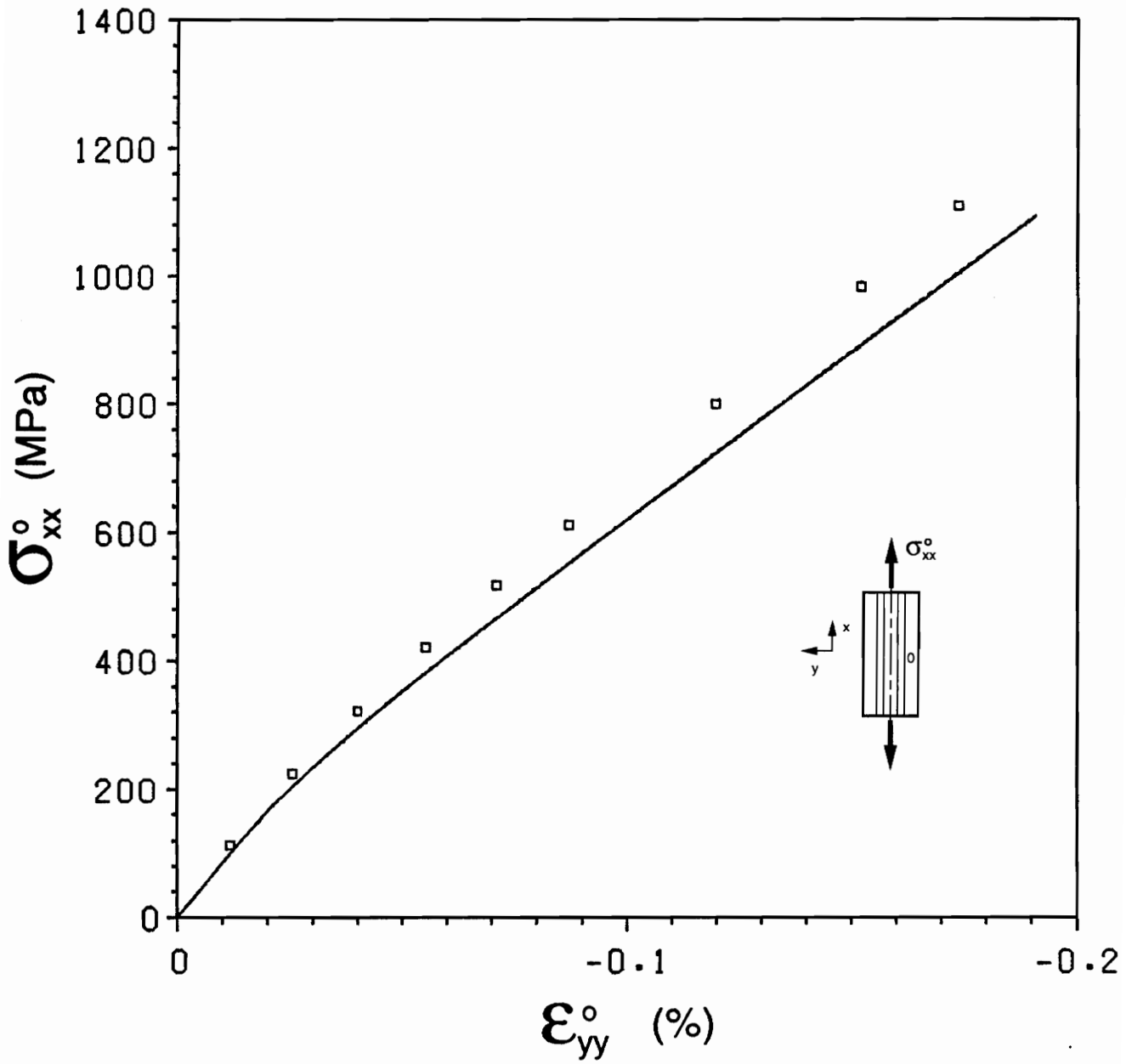

Figure 17. **Transverse response of 0° specimen:** The broken line represents the prediction of the 12 d.o.f. mini grid, while the continuous line represents the prediction of the reference model. The squares correspond to experimental data from [30].

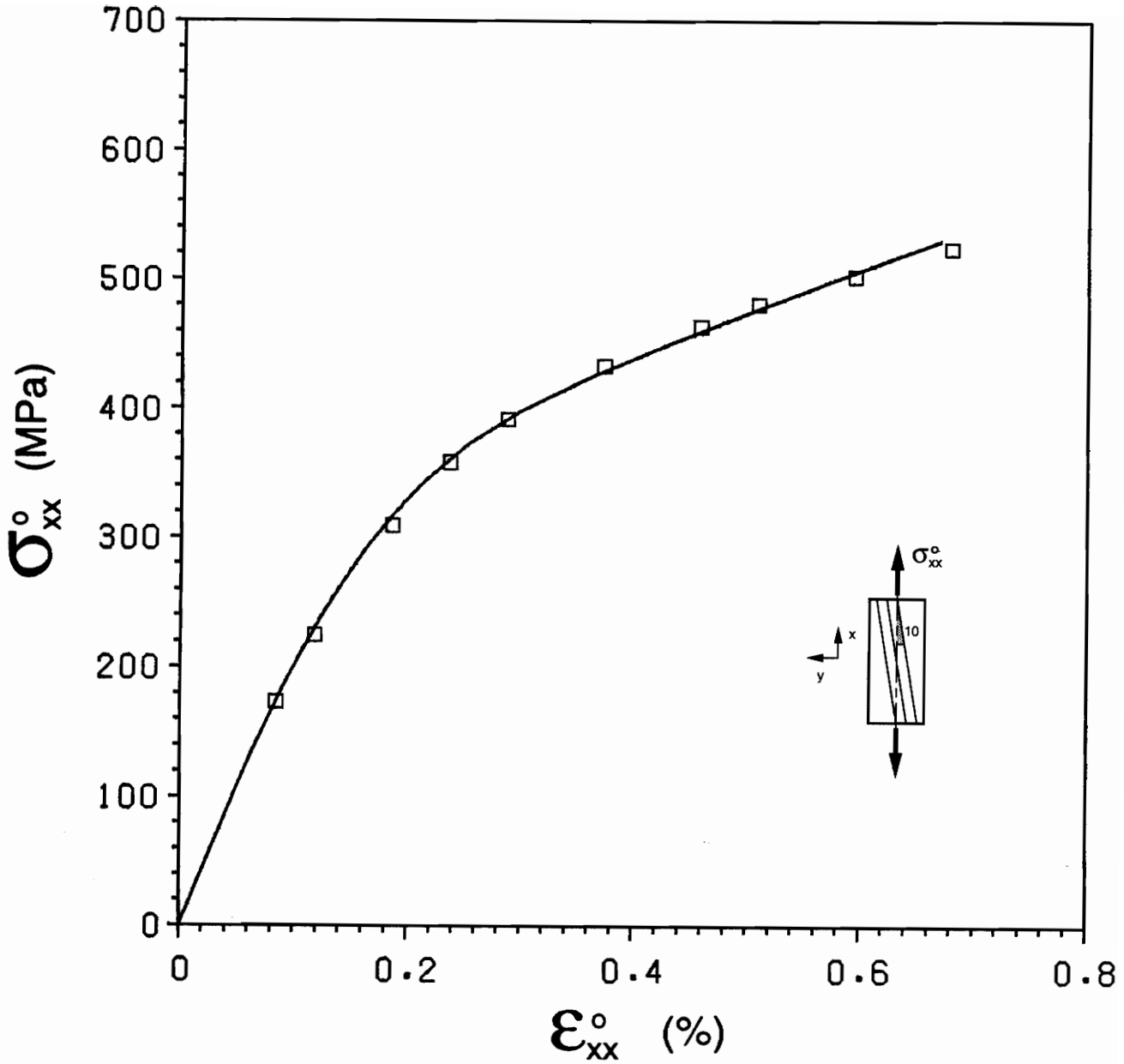

Figure 18. Axial response of 10° specimen: The broken line represents the prediction of the 12 d.o.f. mini grid, while the continuous line represents the prediction of the reference model. The squares correspond to experimental data from [30].

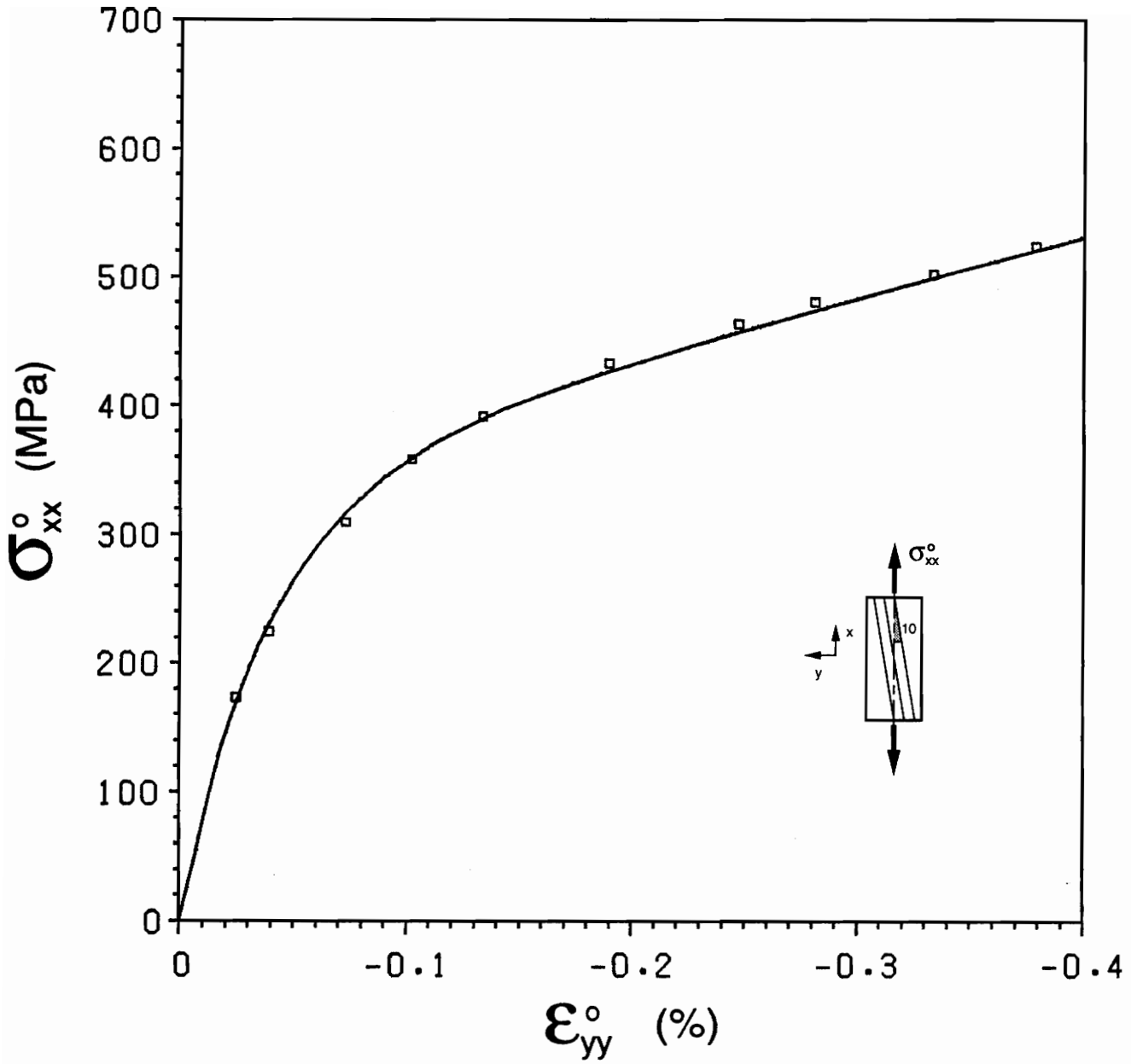

Figure 19. Transverse response of 10° specimen: The broken line represents the prediction of the 12 d.o.f. mini grid, while the continuous line represents the prediction of the reference model. The squares correspond to experimental data from [30].

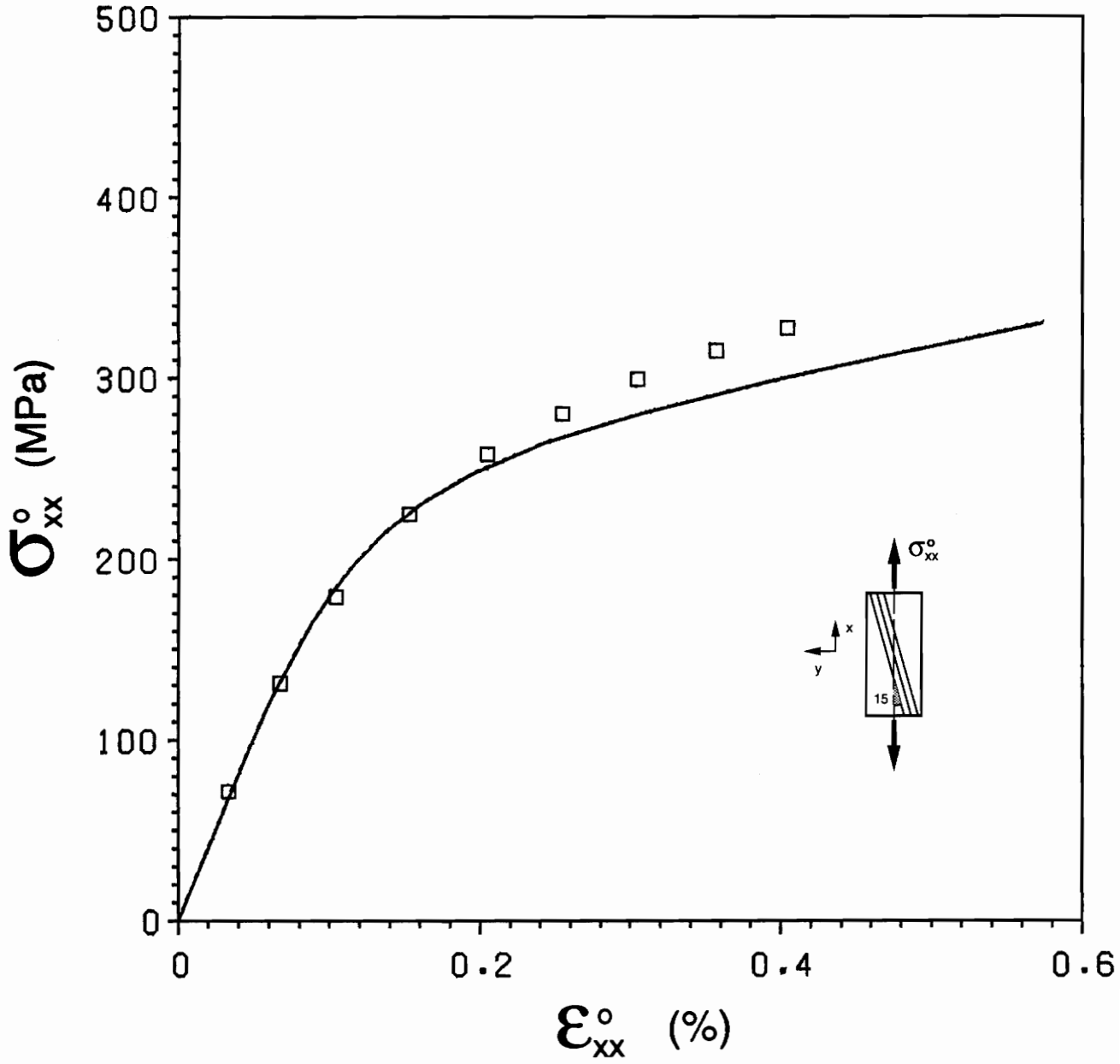

Figure 20. Axial response of 15° specimen: The broken line represents the prediction of the 12 d.o.f. mini grid, while the continuous line represents the prediction of the reference model. The squares correspond to experimental data from [30].

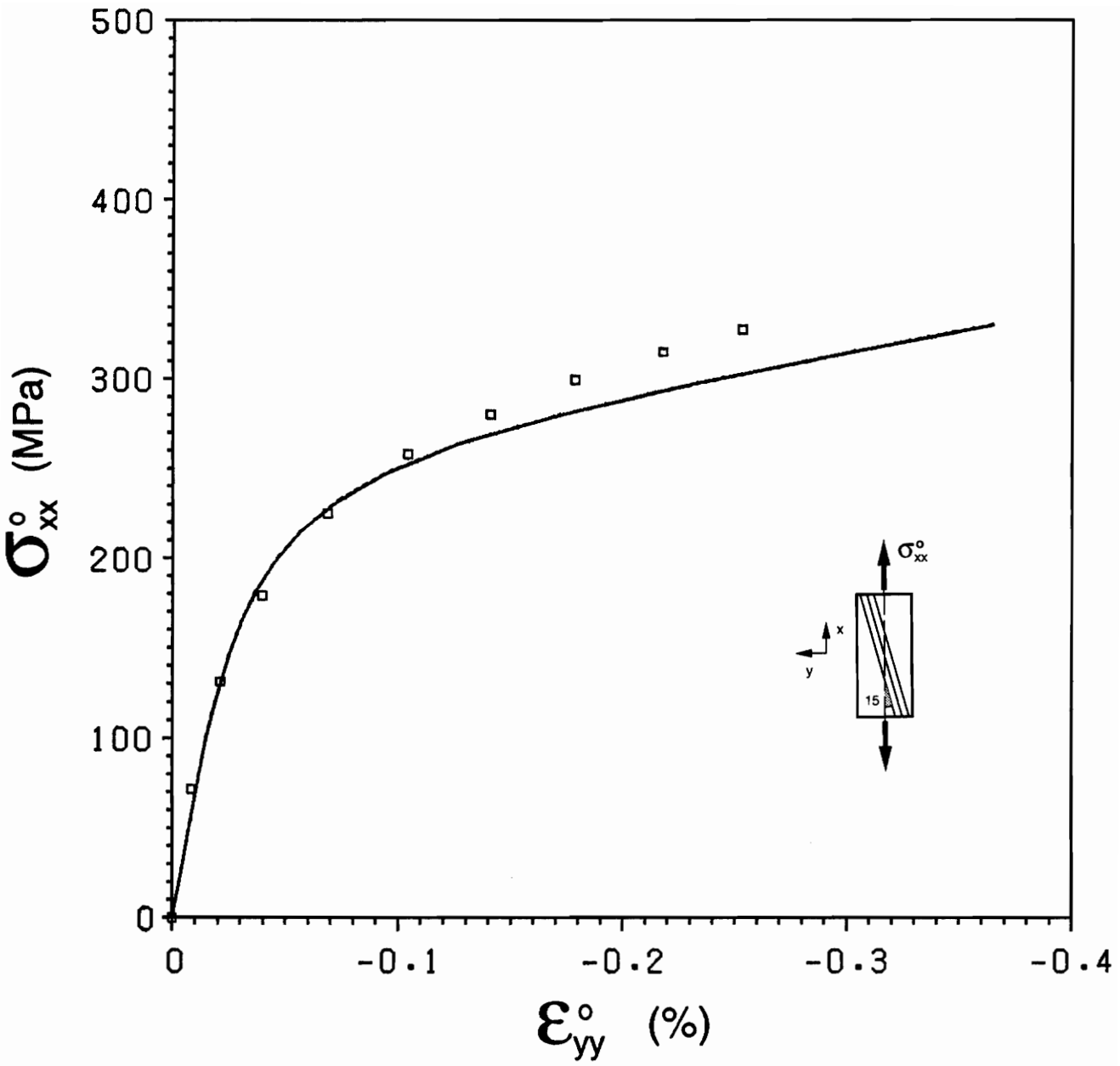

Figure 21. Transverse response of 15° specimen: The broken line represents the prediction of the 12 d.o.f. mini grid, while the continuous line represents the prediction of the reference model. The squares correspond to experimental data from [30].

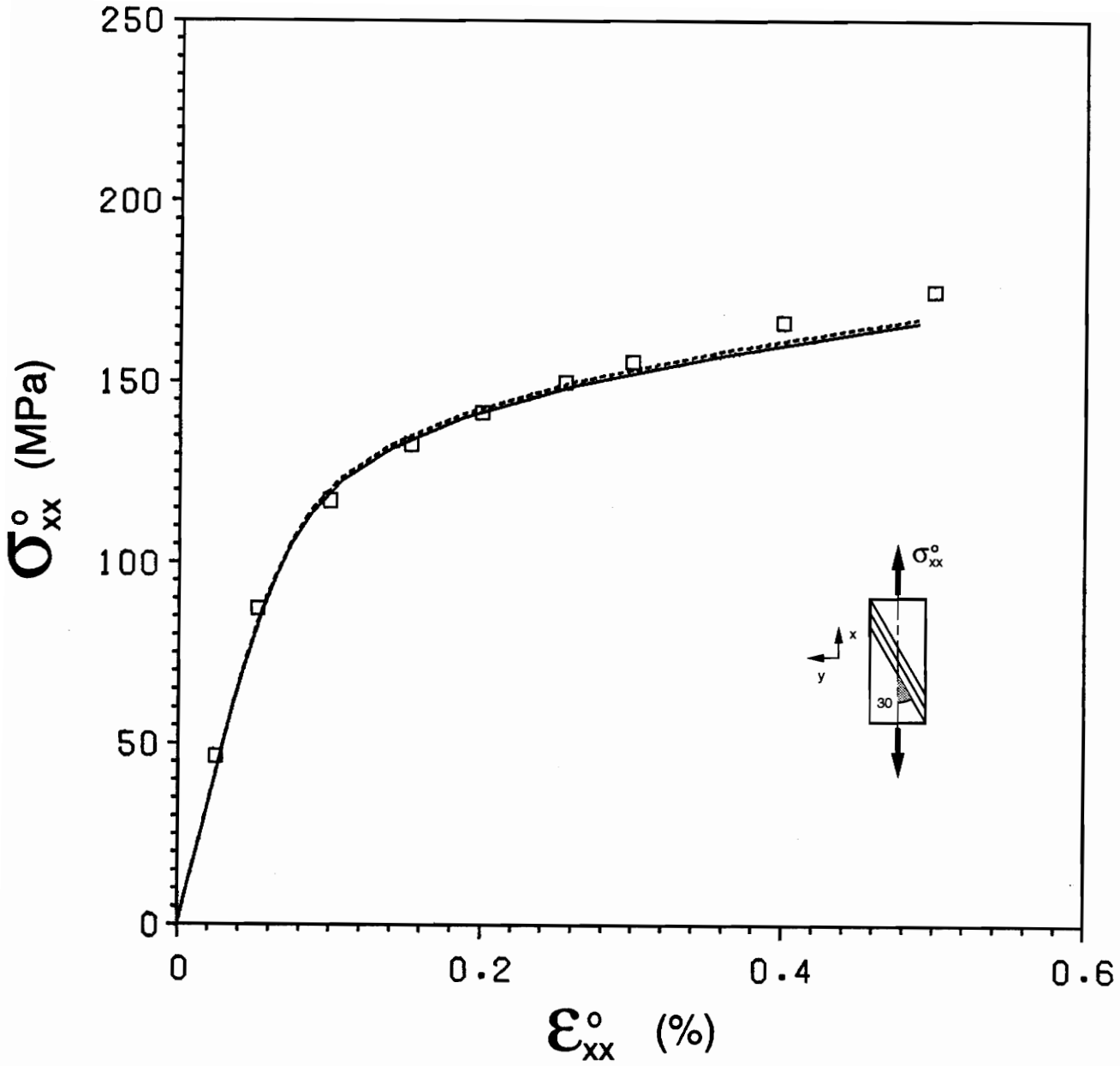

Figure 22. **Axial response of 30° specimen:** The broken line represents the prediction of the 12 d.o.f. mini grid, while the continuous line represents the prediction of the reference model. The squares correspond to experimental data from [30].

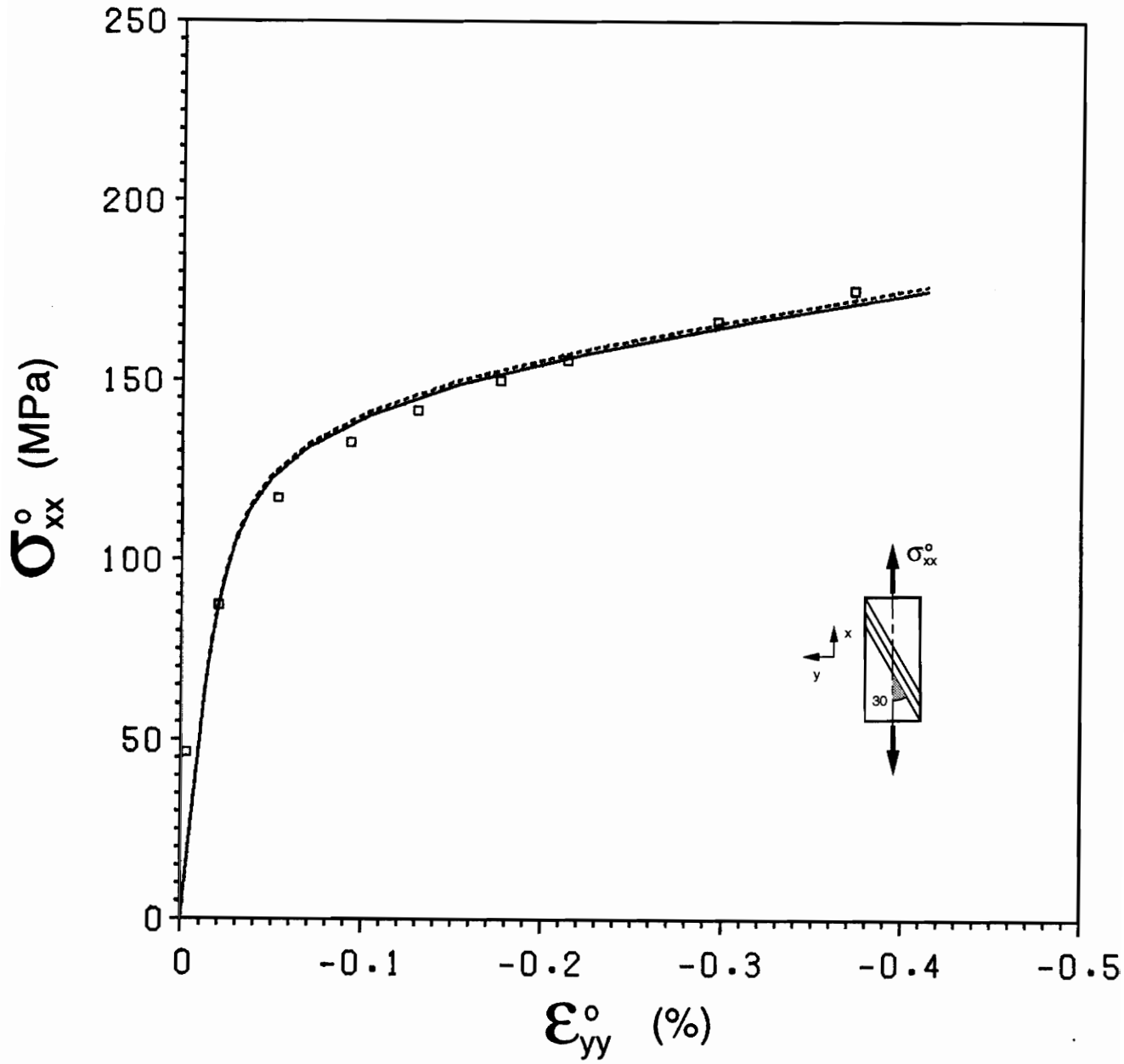

Figure 23. **Transverse response of 30° specimen:** The broken line represents the prediction of the 12 d.o.f. mini grid, while the continuous line represents the prediction of the reference model. The squares correspond to experimental data from [30].

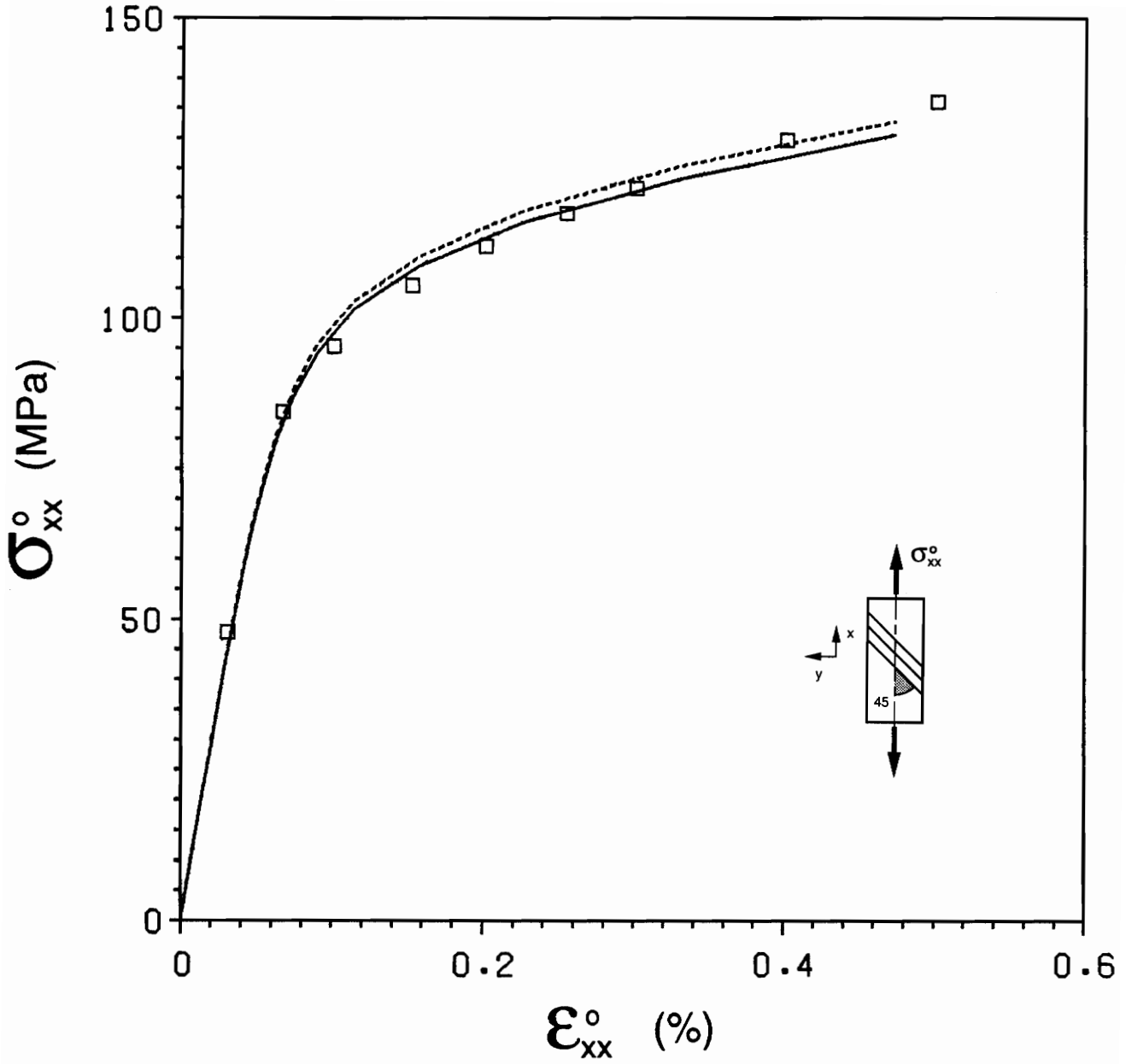

Figure 24. **Axial response of 45° specimen:** The broken line represents the prediction of the 12 d.o.f. mini grid, while the continuous line represents the prediction of the reference model. The squares correspond to experimental data from [30].

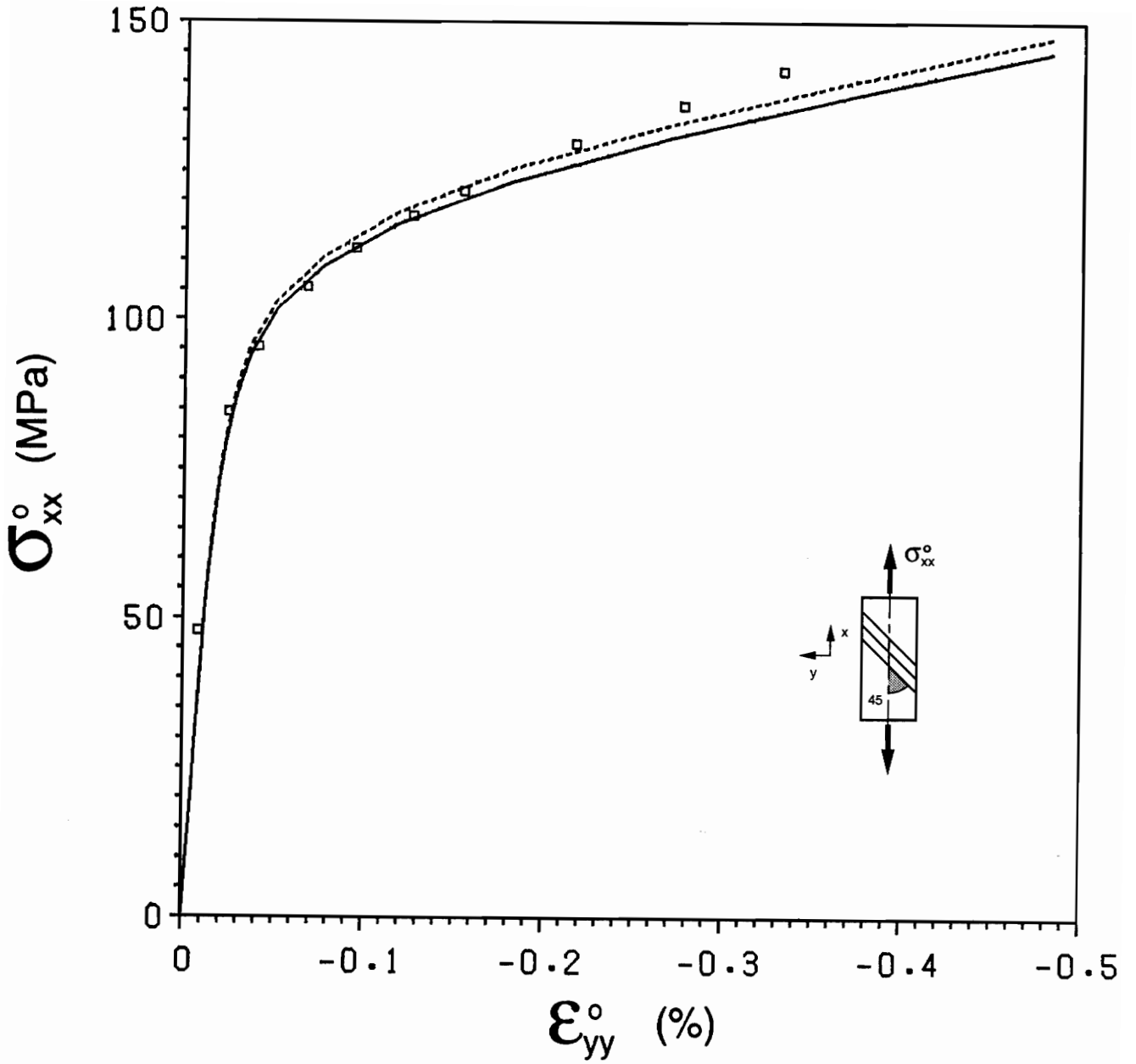

Figure 25. Transverse response of 45° specimen: The broken line represents the prediction of the 12 d.o.f. mini grid, while the continuous line represents the prediction of the reference model. The squares correspond to experimental data from [30].

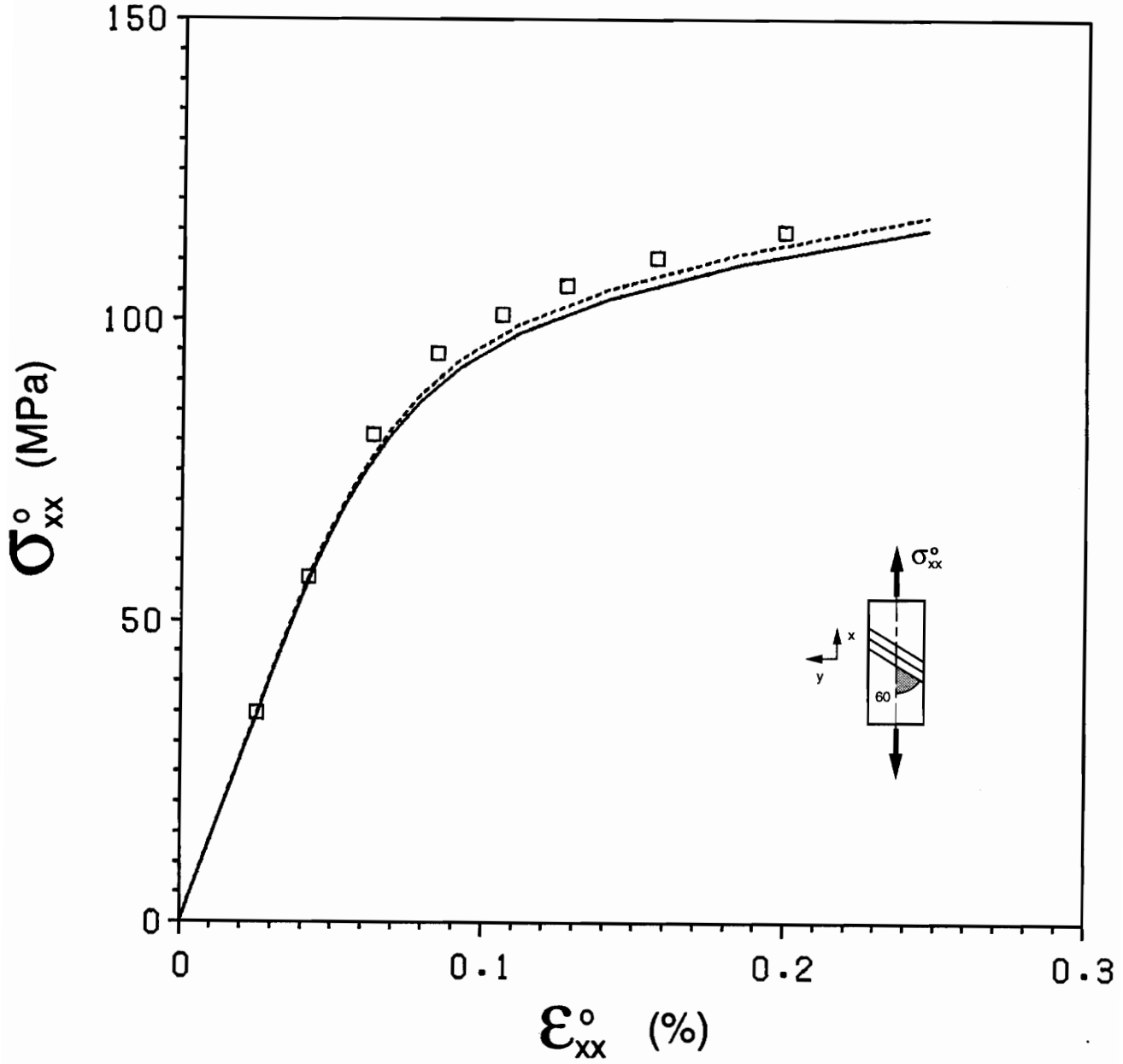

Figure 26. **Axial response of 60° specimen:** The broken line represents the prediction of the 12 d.o.f. mini grid, while the continuous line represents the prediction of the reference model. The squares correspond to experimental data from [30].

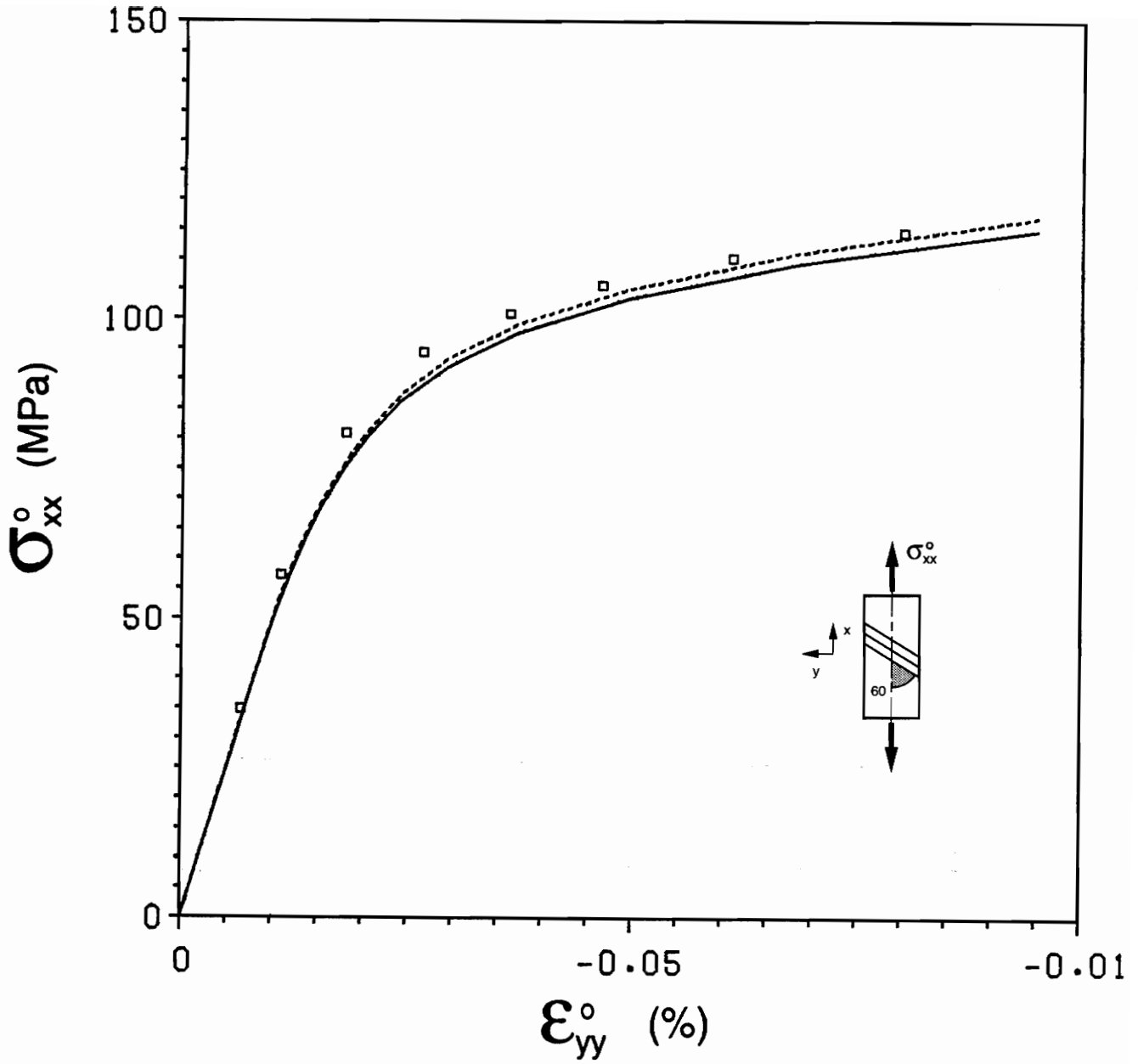

Figure 27. Transverse response of 60° specimen: The broken line represents the prediction of the 12 d.o.f. mini grid, while the continuous line represents the prediction of the reference model. The squares correspond to experimental data from [30].

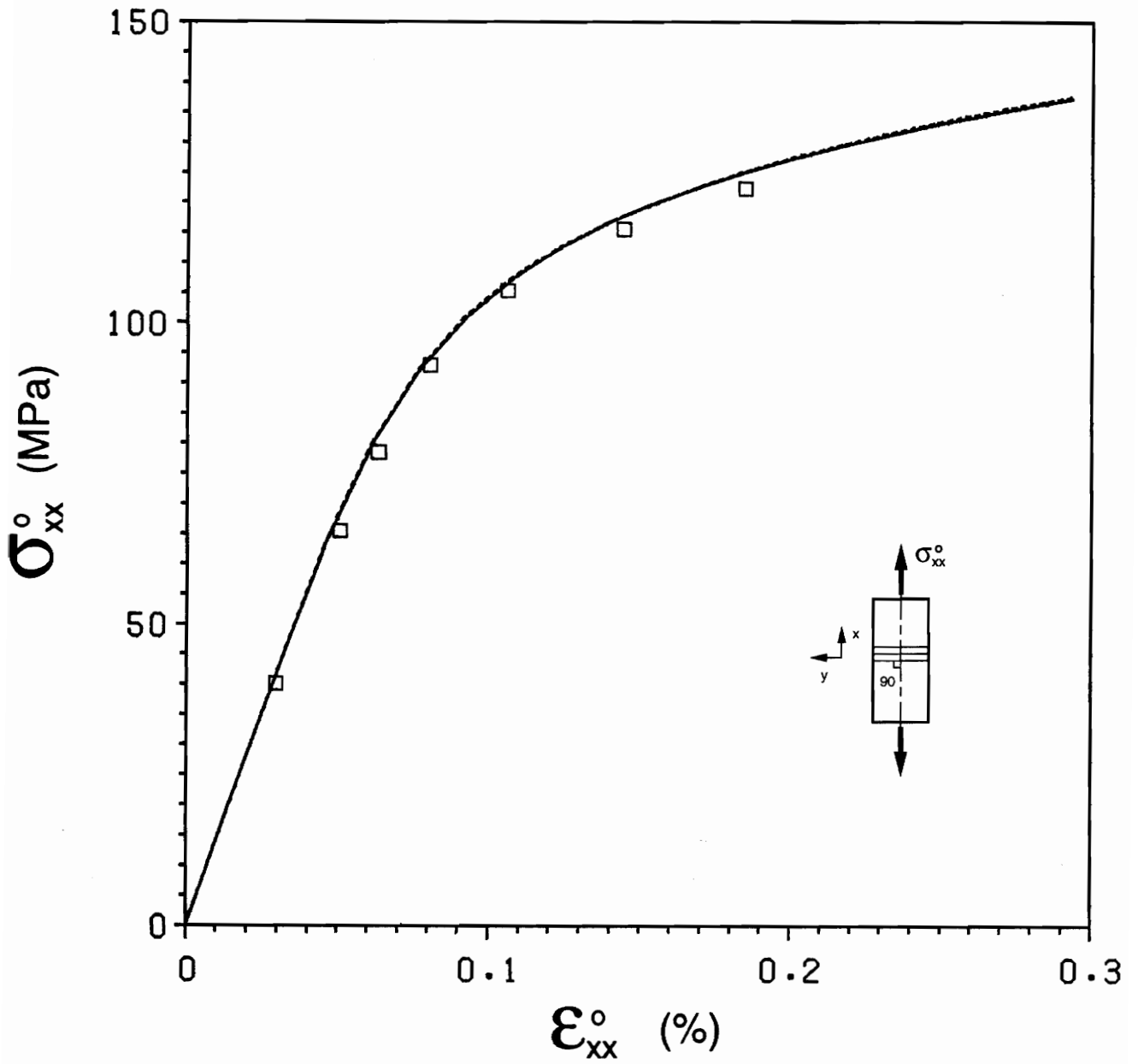

Figure 28. Axial response of 90° specimen: The broken line represents the prediction of the 12 d.o.f. mini grid, while the continuous line represents the prediction of the reference model. The squares correspond to experimental data from [30].

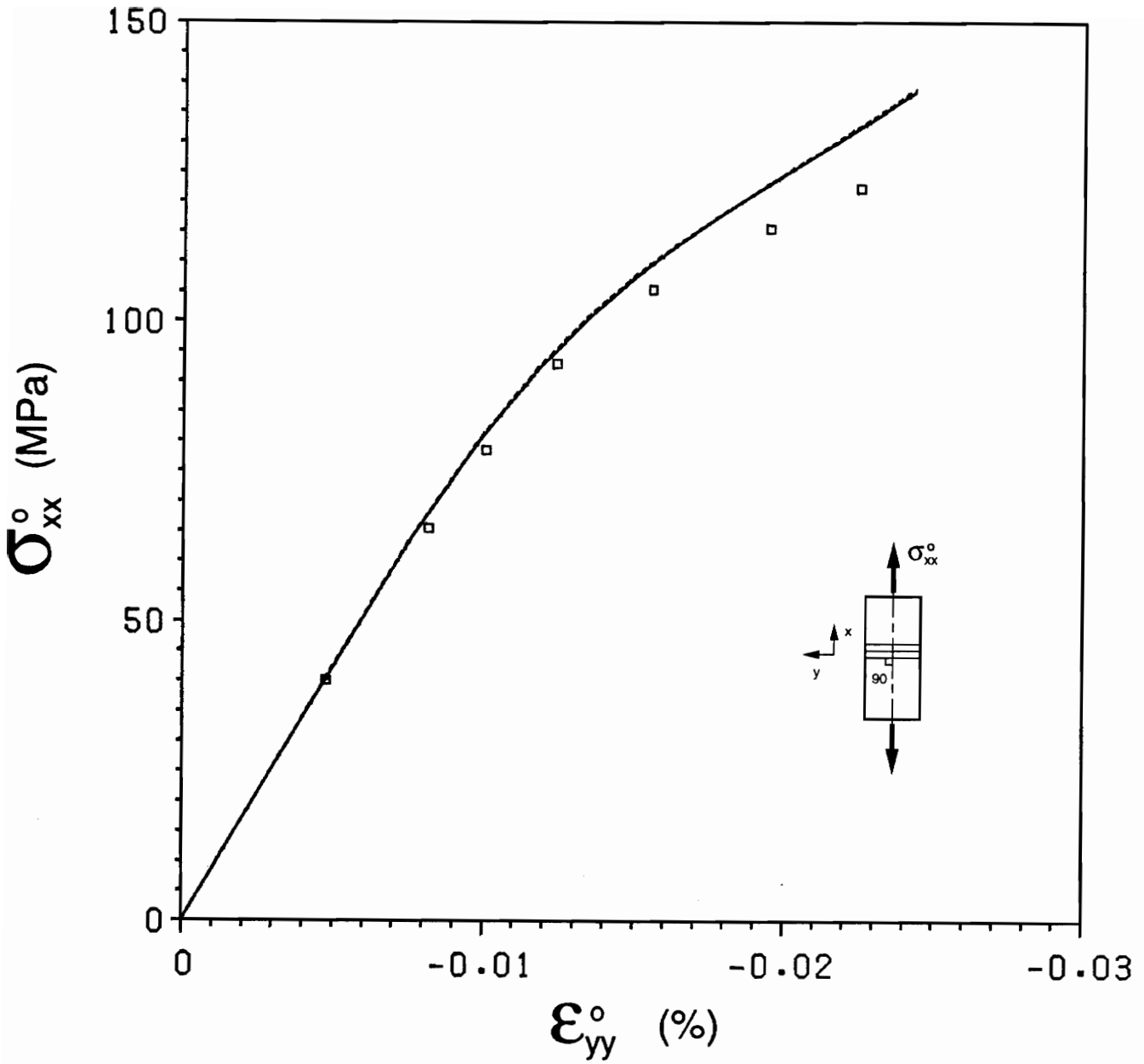

Figure 29. Transverse response of 90° specimen: The broken line represents the prediction of the 12 d.o.f. mini grid, while the continuous line represents the prediction of the reference model. The squares correspond to experimental data from [30].

In all simulations shown in Section 6.1, 6.2, and 6.3, the 12 d.o.f. mini grid used about 0.9 CPU seconds on an IBM 3090-300E, compared to about 45 CPU seconds for the reference model. This represents a 50 fold reduction in computational time.

6.4. *Cyclic Loading*

In this section, we predict the response of the boron/aluminum composite previously described to a transverse-normal longitudinal-shear (or "square") cyclic loading path using the 12 d.o.f. mini grid and the reference grid.

The "square" cyclic loading is shown Fig. 30. This simulation is performed using 170 steps.

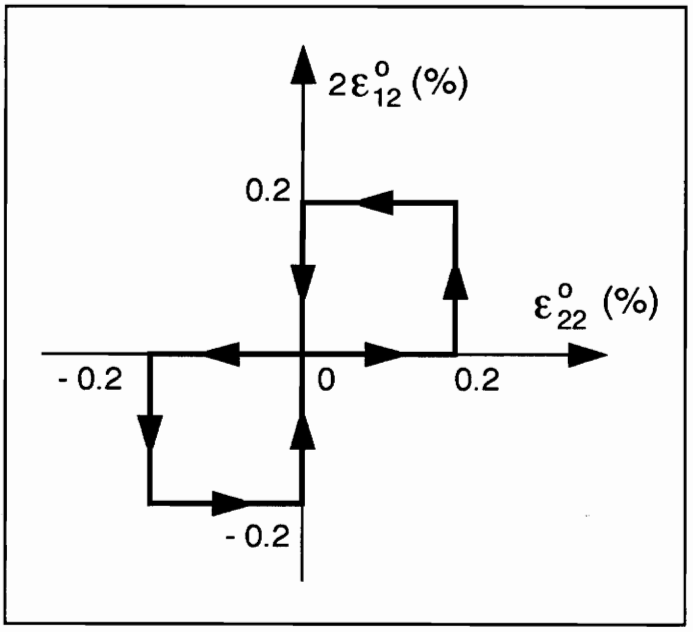

Figure 30. Transverse-normal longitudinal-shear cyclic loading path.

The mini grid predictions are compared to those of the reference grid (Figs. 31-33). On these figures, the broken line represents the prediction of the 12 d.o.f. mini grid, while the diamonds represent the prediction of the reference grid. Very good agreement is again observed and the simulation using the mini grid require 5.5 CPU seconds on an IBM 3090-300E, compared to about 31.6 CPU seconds for the reference grid.

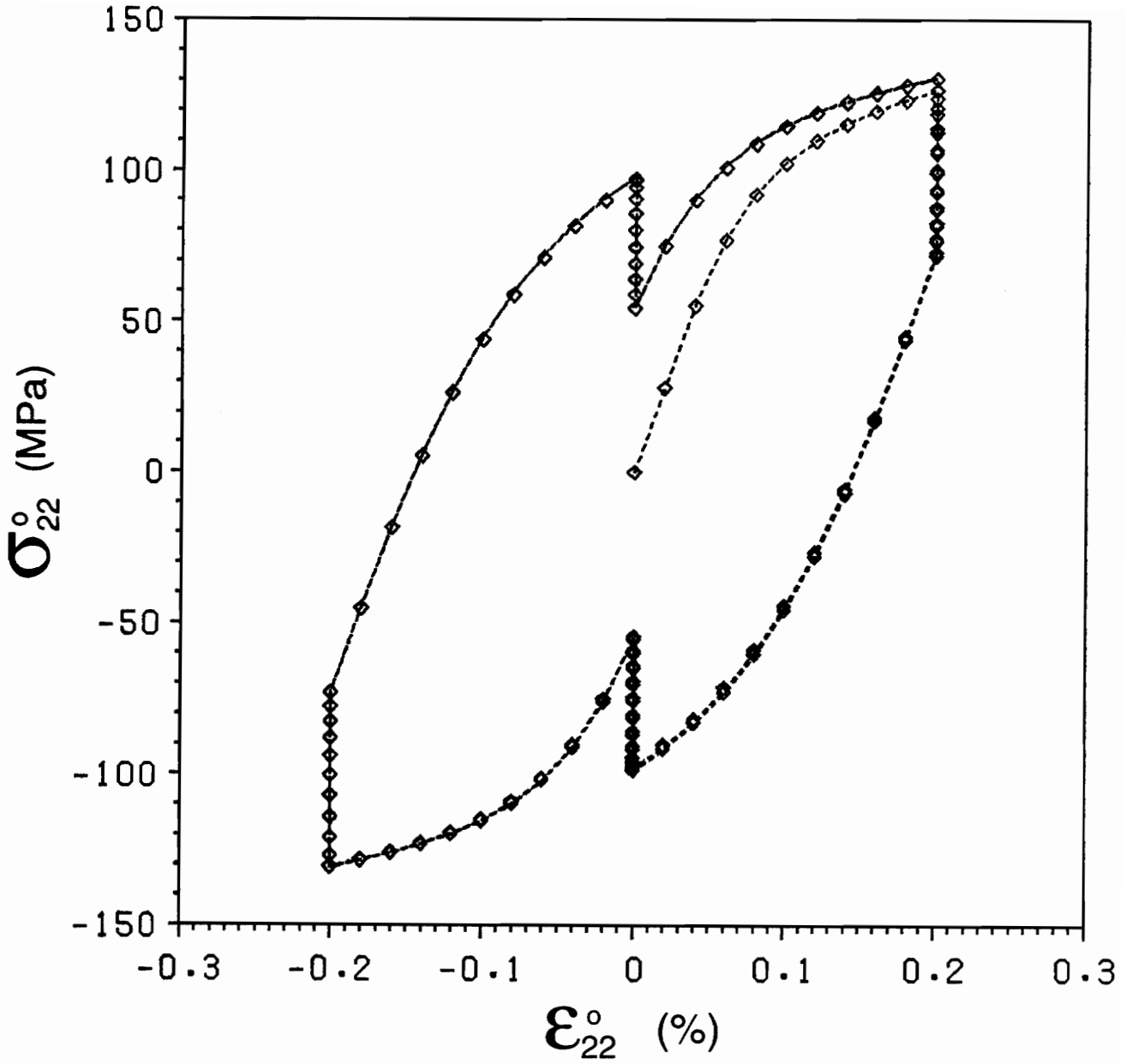

Figure 31. Response to transverse-normal longitudinal-shear cyclic loading: The broken line represents the prediction of the 12 d.o.f. mini grid, while the diamonds represent the prediction of the reference model. Two cycles are shown.

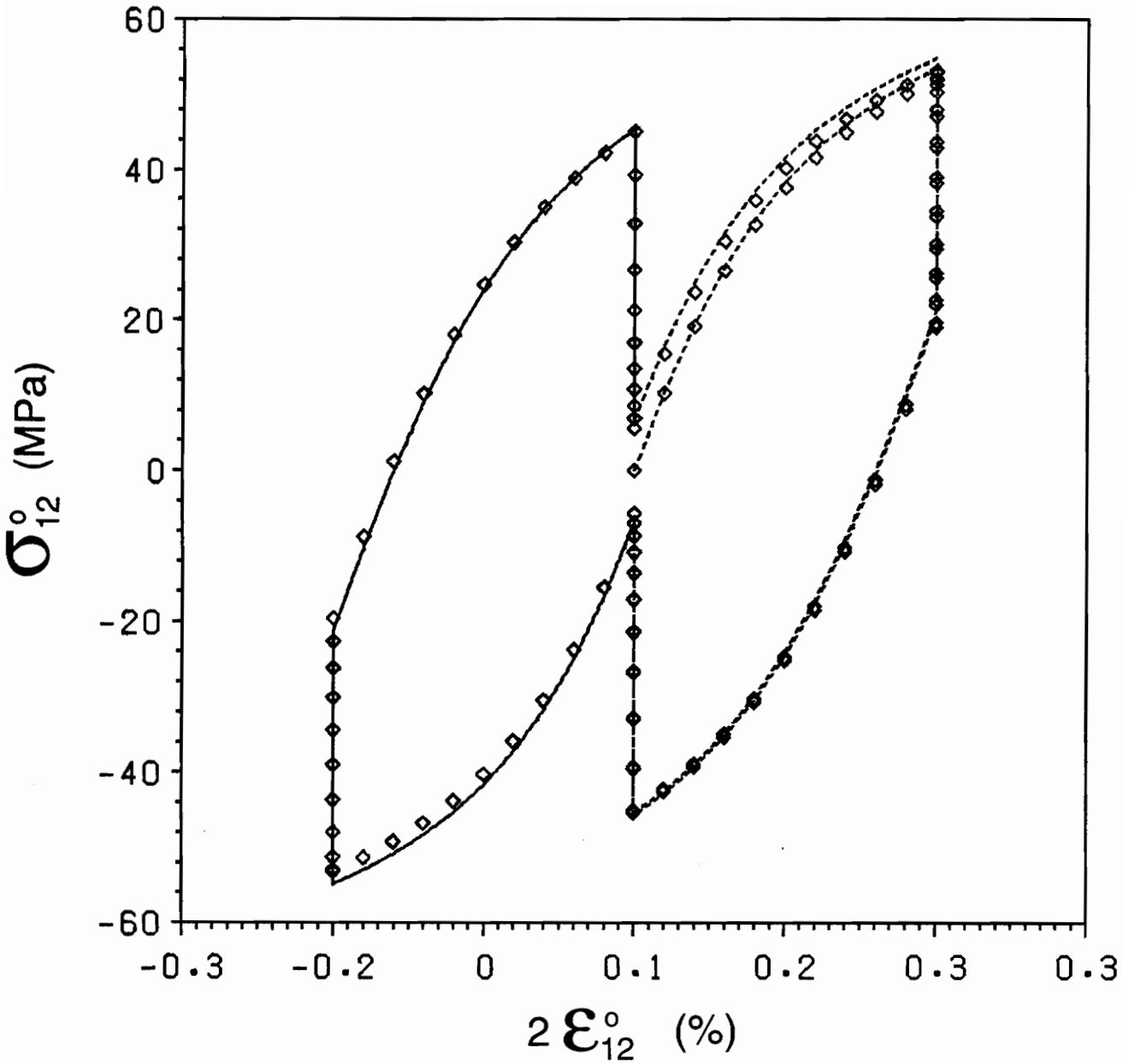

Figure 32. **Response to transverse-normal longitudinal-shear cyclic loading:** The broken line represents the prediction of the 12 d.o.f. mini grid, while the diamonds represent the prediction of the reference model. Two cycles are shown.

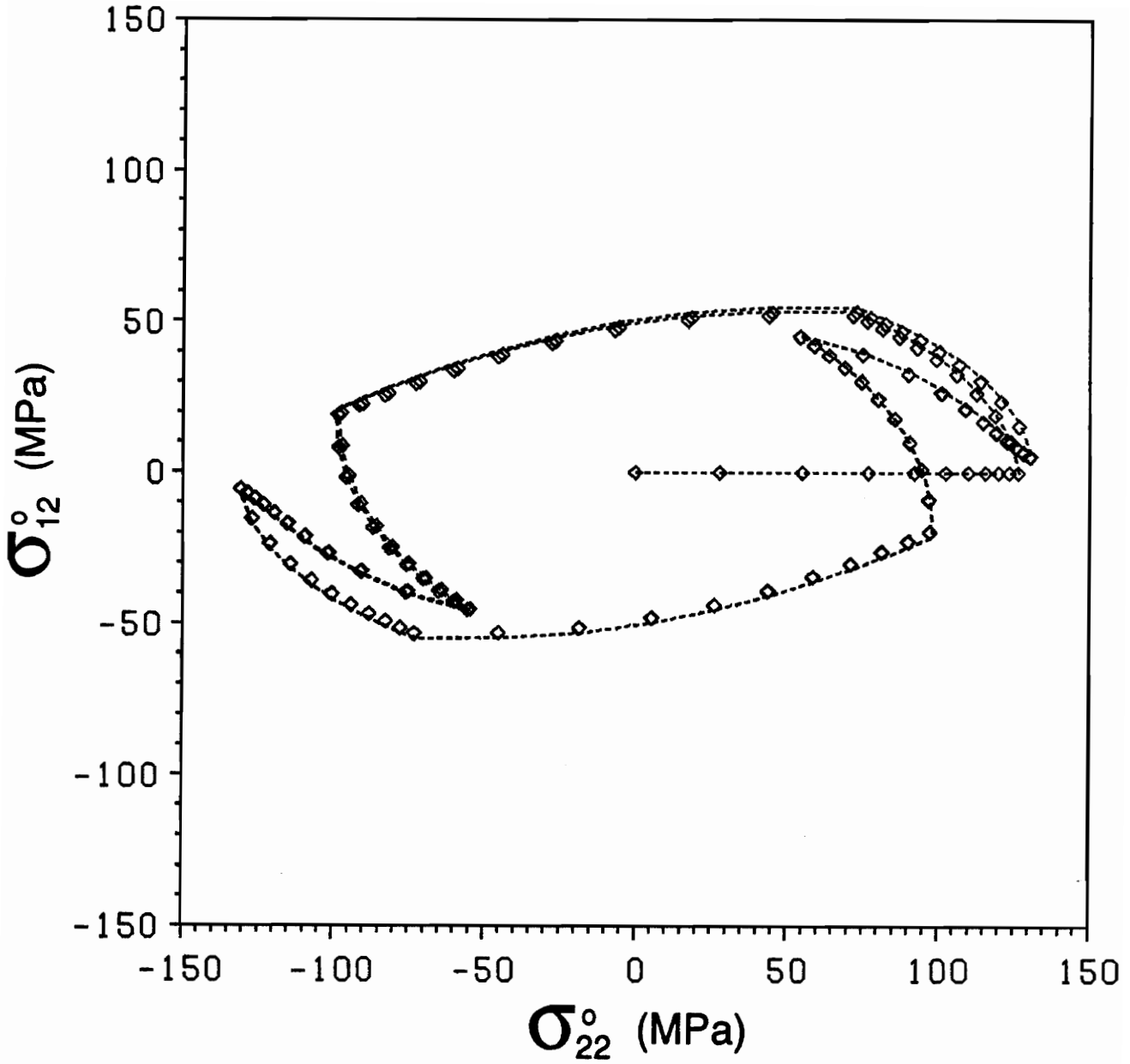

Figure 33. Response to transverse-normal longitudinal-shear cyclic loading: The broken line represents the prediction of the 12 d.o.f. mini grid, while the diamonds represent the prediction of the reference model. Two cycles are shown.

7. Concluding Remarks

A mini finite element micromechanics model involving very few d.o.f. (12 to 18) has been developed to predict elastic-plastic response of unidirectional fiber-reinforced composites under plane stress loading. The plastic behavior of the matrix was modeled using the endochronic constitutive theory for plastically incompressible rate-independent isotropic materials.

A 318 d.o.f. finite element grid using the same unit cell, the same superposition method for the displacement field, the same boundary conditions and the same plastic model for the matrix was used to evaluate the performance of the mini model. Comparison with this fine grid finite element solution showed very good results for various elastoplastic characteristics (off-axis tensile tests and transverse-normal longitudinal-shear cyclic loading) for a boron/aluminum composite and proved the effectiveness of the mini model presented. The largest discrepancies observed between the results from the mini grid and the reference grid was only about 5%. Compared to the reference model, the use of the mini grid allows a 50 fold reduction in computational expenses.

This model has the following characteristics:

1. Symmetry and anti-symmetry conditions have been enforced isolating the smallest unit cell for the periodic diamond model. The resulting unit cell corresponds to a quarter of a hexagon. Specific boundary conditions have been established on its sloping edge.

2. The displacement field within the unit cell is discomposed into a uniform macroscopic strain field, which governs the deformation of the composite at the macroscopic level, and a fluctuating field due to the nonhomogeneity at the microscopic level. The resulting global load-displacement relation allows fast determination of the corresponding macroscopic stress field.

3. The fiber has a circular geometry, which models internal geometry more accurately. Uniform strain is assumed within the fiber.

4. Hierarchic quadratic elements are used to discretize the matrix. These elements are proved to be very valuable in the process of minimizing the number of d.o.f. since hierarchic shape functions allow us to switch very easily from quadratic to linear approximation in a particular direction.

5. A simple optimization process is designed to minimize the number of d.o.f. for a particular material system while avoiding grid locking.

6. Strain-displacement matrices at every material point are computed and then modified to account for boundary conditions and results of the d.o.f. minimization in a preprocessor unit.

Further testing is recommended for other materials systems to fully evaluate the performance of the mini model.

The matrix plasticity model could be extended to orthotropic materials. This would allow to predict elastoplastic characteristics of composites such as carbon/carbon.

Finally, this mini model should be implemented within a larger finite element program to study the plastic response of composite structures. Both stability and efficiency of the numerical procedure used to model the plastic behavior of the matrix have been demonstrated by Hsu [19]. Because of the guaranteed stability, it is possible to use large macrostrain increments without risk of divergence. Furthermore, the efficiency of this numerical procedure is such that the number of iterations needed to reach convergence does not grow significantly as the step size is increased. Therefore, when the mini model is implemented as a material subroutine in an integrated macro-micro analysis, large strain increments can be used at the macro-level and sub-incrementation at the micro-level should not be necessary. This advantage together with the small number of degrees of freedom should allow to use the mini model as a tool to perform integrated macro-micro analysis of composite structures.

References

1. Petit, P. H. and Waddoups, M. E. "A Method of Predicting the Nonlinear Behavior of Laminated Composites," *Journal of Composite Materials*, Vol. 3, 1969, pp. 2 - 19.

2. Hahn, H. T., "Nonlinear Behavior of Laminated Composites," *Journal of Composite Materials*, Vol. 7, 1973, pp. 257 - 271.

3. Hashin, Z. D., Bagchi, D., and Rosen, B. W., "Nonlinear Behavior of Fiber Composite Laminates," *NASA CR-213 (1974)*.

4. Sandhu, R. S., "Nonlinear Behavior of Unidirectional and Angle-Ply Laminates," *Journal of Aircraft*, Vol. 13, 1974, pp. 104 - 111.

5. Jones, R. M., and Morgan, H. S., "Analysis of Nonlinear Stress-Strain Behavior of Fiber-Reinforced Composite Materials," *AIAA Journal*, Vol. 15, 1977, pp. 1669 - 1676.

6. Amijima, S., and Adachi, T., "Nonlinear Stress-Strain Response of Laminated Composites," *Journal of Composite Materials*, Vol. 13, 1979, pp. 206 - 218.

7. Griffin, O. H., Jr., Kamat, M. P., and Herakovich, C. T., "Three-Dimensional Inelastic Finite Element Analysis of Laminated Composites," *Journal of Composite Materials*, Vol. 15, 1981, pp. 543 - 560.

8. Nahas, M. N., "Analysis of Nonlinear Stress-Strain Response of Laminated Fiber-Reinforced Composites," *Fiber Science and Technology*, Vol. 20, 1984, pp. 297 - 313.

9. Hashin, Z. and Rosen, B. W., "The Elastic Moduli of Fiber-Reinforced Material," *Journal of Applied Mechanics*, Vol. 31, 1964, pp. 223 - 232.

10. Dvorak, G. J., and Rao, M. S., "Axisymmetric Plasticity Theory of Fibrous Composites," *International Journal of Engineering Science*, Vol. 14, 1976, pp. 361 - 373.

11. Hershey, A. V., " The Elasticity of an Isotropic Aggregate of Anisotropic Cubic Crystals," *Journal of Applied Mechanics*, Vol. 21, 1954, pp. 236 - 240.

12. Eshelby, J. D., "The Determination of the Elastic Field of an Ellipsoidal Inclusion and Related Problems," *Proceedings of the Royal London Society*, Vol. 241, 1957, pp. 376 - 396.

13. Hill, R., "Continuum Micro-Mechanics of Elastoplastic Polycrystal," *Journal of the Mechanics and Physics of Solids*, Vol. 13, 1965, pp. 89 - 101.

14. Budiansky, B., "On the Elastic Moduli of Some Heterogeneous Materials," *Journal of the Mechanics and Physics of Solids*, Vol. 27, 1979, pp. 51 - 72.

15. Dvorak, G. J., and Bahei-El-Din, Y. A., "Elastic-plastic Behavior of Fibrous Composites," *Journal of the Mechanics and Physics of Solids*, Vol. 27, 1979, pp. 51 - 72.

16. Hutchinson, J. W., "Elastic-plastic Behavior of Polycrystalline Metals and Composites," *Proceedings of the Royal London Society*, Vol. 319, 1970, pp. 247 - 272.

17. Dvorak, G. J., and Bahei-El-Din, Y. A., "Plasticity Analysis of Fibrous Composites," *Journal of Applied Mechanics*, Vol. 49, 1982, pp. 327 - 335.

18. Aboudi, J., "Elastoplasticity Theory for Composite Materials," *Solid Mechanics Archives*, Vol. 11, No. 3, 1986, pp. 141 - 183.

19. Hsu, S. Y., "Finite Element Micromechanics Modeling of Inelastic Deformation of Unidirectionally Fiber-Reinforced Composites," Ph.D. Dissertation, Virginia Polytechnic Institute and State University, Blacksburg, VA, 1992.

20. Pindera, M. J., and Aboudi, J., "Micromechanical Analysis of Yielding of Metal Matrix Composites," *International Journal of Plasticity*, Vol. 4, 1988, pp. 195 - 214.

21. Aboudi, J., "Closed Form Constitutive Equations for Metal Matrix Composites," *International Journal of Engineering Science*, Vol. 25, No. 9, 1987, pp. 1229 - 1240.

22. Pindera, M. J., Herakovich, C. T., Becker, W., and Aboudi, J., "Nonlinear Response of Unidirectional Boron/Aluminum," *Journal of Composite Materials*, Vol. 24, 1990, pp. 2 - 21.

23. Arenburg, R. T., and Reddy, J. N. "Analysis of Metal-Matrix Composite Structures - II. Laminate Analyses," *Computers and Structures*, Vol. 40, 1991, pp. 1369 - 1385.

24. Sun, C. T., and Chen, J. L. "A Micromechanical Model for Plastic Behavior of Fibrous Composites," *Journal of Composites Sciences and Technology*, Vol. 40, 1991, pp. 115 - 129.

25. Adams, D. F., "Inelastic Analysis of a Unidirectional Composite Subjected to Transverse Normal Loading," *Journal of Composite Materials*, Vol. 4, 1970, pp. 310 - 328.

26. Foye, R. L., "Theoretical Post-Yielding Behavior of Composite Laminates - I. Inelastic Micromechanics," *Journal of Composite Materials*, Vol. 7, 1973, pp. 178 - 193.

27. Jansson, S., "Mechanical Characterization and Modeling of Non-linear Deformation and Fracture of a Fiber Reinforced Metal Matrix Composite," *Journal of Mechanics of Materials*, Vol. 12, 1991, pp. 47 - 62.

28. Teply, J. L. and Dvorak, G. J., "Dual Estimates of Overall Instantaneous Properties of Elastic-Plastic Composites," Proceedings, *5th International Symposium on Continuum Models of Discrete Systems*, Spencer, A. J. M., ed., Nottingham, UK, 1985, pp. 205 - 216.

29. Teply, J. L. and Dvorak, G. J., "Bounds on Overall Instantaneous Properties of Elastic-Plastic Composites," *Journal of the Mechanics and Physics of Solids*, Vol. 36, No. 1, 1988, pp. 29 - 58.

30. Becker, W., Pindera, M. J., and Herakovich, C. T., "Mechanical Response of Unidirectional Boron/Aluminum under Combined Loading," Technical Report VPI-E-81-17, College of Engineering, Virginia Polytechnic Institute and State University, Blacksburg, Virginia, 1987.

31. Zienkiewicz, O. C., and Taylor, R. L., "The Finite Element Method, Fourth Edition," Section 7.2., Mc Graw-Hill Book Company, Maidenhead, Berkshire, UK, 1989.

32. Valanis, K. C., "A Theory of Viscoplasticity Without a Yield Surface, Part I. General Theory," *Archives of Mechanics*, Vol. 23, 1971, pp. 517 - 534.

33. Valanis, K. C., "Fundamental Consequences of a New Intrinsic Time Measure: Plasticity as a Limit of the Endochronic Theory," *Archives of Mechanics*, Vol. 32, 1980, pp. 171 - 191.

34. Valanis, K. C., "Continuum Foundations of Endochronic Plasticity," *Journal of Engineering Materials and Technology*, Vol. 106, 1984, pp. 367 - 375.

Appendix A. Macroscopic Stress Field

Let us consider the cylindrical volume Ω of axis parallel with $x_1 = 0$ and of axial length L shown in Fig. 4 of Section 2.4. The cross-section of Ω on the $x_1 = 0$ plane corresponds to our unit cell. This unit cell has an area of A, and its contour is denoted by C. The boundary of Ω is denoted by Γ and includes the lateral surfaces and the two ends.

By applying Green's theorem, the third term in Eq. (11) of Section 2.4 becomes

$$\sum_e \int_{\Gamma_e} t_j X_{ij} \, d\Omega = \sum_e \int_{\Omega_e} [\sigma_{jk} X_{ij}]_{,k} \, d\Omega, \qquad (A-1)$$

where

$$X_{ij} = \begin{bmatrix} 0 & x_1 & 0 & x_2 \\ 0 & 0 & x_2 & 0 \\ x_3 & 0 & 0 & 0 \end{bmatrix} \qquad (A-2)$$

is a matrix containing the spatial coordinates (x_1,x_2,x_3) of the point where the surface tractions t_j are evaluated and σ_{jk} defines the stress state at this point. Note that the summation symbol indicate that we include contributions from all the elements e of Γ of surface Γ_e, and from all the elements e of Ω of volume Ω_e. Eq. (A-1) further reduces to

$$\sum_{e} \int_{\Omega_e} [\sigma_{ik,k} X_{ij} + \delta_{ij} \sigma_{ik}] \, d\Omega. \qquad (A-3)$$

The first term in Eq. (A-3) vanishes by equilibrium and we obtain

$$\sum_{e} \int_{\Omega_e} \sigma_{ij} \, d\Omega = \int_{\Omega} \sigma_{ij} \, d\Omega. \qquad (A-4)$$

If we define the macroscopic plane stress field σ_{ij}° as the average plane stress field over the cylindrical volume Ω, we can write

$$\sigma_{ij}^{\circ} = \frac{\int_{\Omega} \sigma_{ij} d\Omega}{\int_{\Gamma} dV} = \frac{\int_{\Omega} \sigma_{ij} d\Omega}{A\,L}, \qquad (A-5)$$

and the third term of Eq. (11) reduces to $\boldsymbol{\sigma}^{\circ} A\,L$.

Appendix B. Interpolation Functions and Strain-Displacement Relation Matrices

1. Matrix Elements

Elements I, II and III of the mini model discretizing the matrix are hierarchic elements similar to the one shown in Fig. 34.

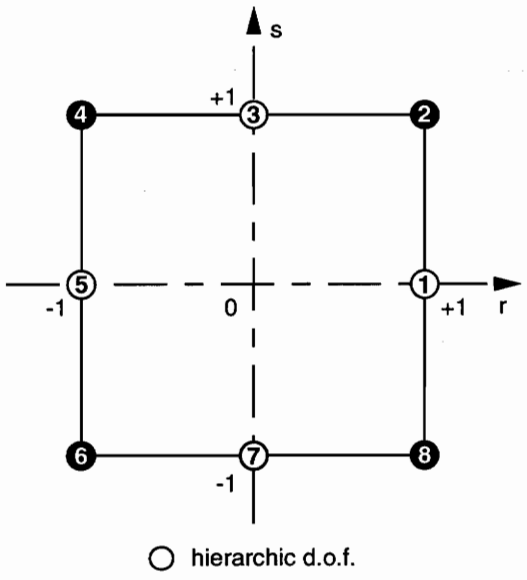

Figure 34. 2-D hierarchic element.

The first order hierarchic interpolation functions for this type of element in the local coordinate system (r,s) are as follows:

$$N_1 = -\frac{1}{2}(s^2 - 1)(1 + r), \qquad (B-1)$$

$$N_2 = \frac{1}{4}(1 + r)(1 + s), \qquad (B-2)$$

$$N_3 = -\frac{1}{2}(r^2 - 1)(1 + s), \qquad (B-3)$$

$$N_4 = \frac{1}{4}(1 - r)(1 + s), \qquad (B-4)$$

$$N_5 = -\frac{1}{2}(s^2 - 1)(1 - r), \qquad (B-5)$$

$$N_6 = \frac{1}{4}(1 - r)(1 - s), \qquad (B-6)$$

$$N_7 = -\frac{1}{2}(r^2 - 1)(1 - s), \qquad (B-7)$$

and

$$N_8 = \frac{1}{4}(1 + r)(1 - s). \qquad (B-8)$$

Nodes 1, 3, 5 and 7 of coordinates x_i are associated with hierarchic interpolation functions and require a particular mapping. Those located along straight edges do not need any mapping, while those located on the fiber-matrix interface (curved edge) are mapped to

$$x_i - \frac{x_{i+1} + x_{i-1}}{2}, \qquad (B-9)$$

where x_i denotes the global coordinates of the hierarchic node-i, and x_{i+1} and x_{i-1} the global coordinates of the two adjacent nodes.

The standard B matrix defined in Eq. (6) is for this element a 6×24 matrix and is given in the global coordinate system (x_1,x_2,x_3) by

$$\mathbf{B} = \mathbf{L}\,[\mathbf{I}N_1 \;\; \mathbf{I}N_2 \;\; .... \;\; \mathbf{I}N_8], \qquad (B-10)$$

where **L** is the differential operator defined in Eq. (8) of Section 2.4, **I** is the 3×3 identity matrix and the N_i are the 8 interpolations functions. Eq. (B-10) can be rewritten as

$$\mathbf{B} = [\mathbf{B}_1 \;\; \mathbf{B}_2 \;\; .... \;\; \mathbf{B}_8], \qquad (B-11)$$

where

$$\mathbf{B}_i = \begin{bmatrix} \frac{\partial N_i}{\partial x_1} & 0 & 0 \\ 0 & \frac{\partial N_i}{\partial x_2} & 0 \\ 0 & 0 & \frac{\partial N_i}{\partial x_3} \\ 0 & \frac{\partial N_i}{\partial x_3} & \frac{\partial N_i}{\partial x_2} \\ \frac{\partial N_i}{\partial x_3} & 0 & \frac{\partial N_i}{\partial x_1} \\ \frac{\partial N_i}{\partial x_2} & \frac{\partial N_i}{\partial x_1} & 0 \end{bmatrix}. \qquad (B-12)$$

2. *Fiber*

The B matrix for the fiber (element IV) is simply given by

$$\mathbf{B}_{IV} = \mathbf{L}\,\mathbf{N}_{IV} = \begin{bmatrix} 0 & 0 & 0 \\ 1 & 0 & 0 \\ 0 & 1 & 0 \\ 0 & 0 & 0 \\ 0 & 0 & 0 \\ 0 & 0 & 1 \end{bmatrix}, \qquad (B-13)$$

where **L** is the 6x3 differential operator previously defined and $\mathbf{N}_{IV}$ is the shape function matrix for the fiber given by Eq. (26) of Section 4.2:

$$\mathbf{N}_{IV} = \begin{bmatrix} 0 & 0 & x_2 \\ x_2 & 0 & 0 \\ 0 & x_3 & 0 \end{bmatrix}. \qquad (B-14)$$

Appendix C. Endochronic Plasticity Model

1. Endochronic Constitutive Equation Integration

The endochronic theory was first introduced by Valanis [32] in 1971. It is based on the laws of irreversible thermodynamics and provides a unified approach for describing elastoplastic behavior of materials. It does not involve the notion of a yield surface nor the specification of a function to distinguish loading from unloading events.

For rate-independent plastically incompressible isotropic materials which do not exhibit significant hardening, the endochronic constitutive equation is given by [33]

$$s_{ij} = \int_0^z \rho(z - z') \frac{d\varepsilon_{ij}^p}{dz'} dz', \qquad (C-1)$$

where z is the so-called intrinsic time defined by

$$dz = (d\varepsilon_{ij}^p d\varepsilon_{ij}^p)^{1/2}, \qquad (C-2)$$

s_{ij} is the deviatoric stress tensor, ε_{ij}^p is the plastic strain tensor, and $\rho(z)$ denotes the hereditary function which is weakly singular at $z = 0$.

If no yield surface is considered, it has been shown that the function $\rho(z)$ may be represented by an n-term Dirichlet series [34],

$$\rho(z) = \sum_{r=1}^{n} C_r e^{-\alpha_r z}. \qquad (C-3)$$

It has also been demonstrated [34] that this function should satisfy a number of requirements: $\rho(0)$ should be sufficiently large in order to insure instantaneous elastic response at initial loading and loading reversals, and material constants C_r and α_r, determined experimentally, should be such that $\alpha_1 = 0$, $C_1 \geq 0$, and α_r and C_r are positive for $r \geq 2$.

The endochronic constitutive equation can be easily integrated. By taking the derivative of this equation with respect to z and viewing the deviatoric stress s_{ij} as the sum of n-terms, $s_{ij} = \sum_{r=1}^{n} s_{ij}^r$, $r = 1, ..., n$, we can derive a first order differential equation which govern the evolution of s_{ij}^r:

$$\frac{ds_{ij}^r}{dz} + \alpha_r s_{ij}^r = C_r \frac{d\varepsilon_{ij}^p}{dz}, \quad r = 1, ..., n. \tag{C-4}$$

The right-hand side of this equation is not constant. Discretizing the loading path into small segments, we can reasonably approximate this term by forward difference as

$$\frac{d\varepsilon_{ij}^p}{dz} = \frac{\Delta\varepsilon_{ij}^p}{\Delta z}, \tag{C-5}$$

where $\Delta\bullet$ denotes the difference between two quantities at the beginning and end of the mth segment (i.e. $\Delta\bullet = \bullet_m - \bullet_{m-1}$). With this approximation, Eq. (C-4) reduces to a first order differential equation with constant coefficients within an interval, and is integrated analytically.

Using the initial condition, $s_{ij}^r = (s_{ij}^r)_{m-1}$ at $z = z_{m-1}$, the solution is

$$(s_{ij}^r)_m = (s_{ij}^r)_{m-1} e^{-\alpha_r \Delta z} + \frac{\Delta\varepsilon_{ij}^p}{\Delta z} \frac{C_r}{\alpha_r} (1 - e^{-\alpha_r \Delta z}). \tag{C-6}$$

Rewriting Eq. (C-6) for the stress increment Δs_{ij}^r in terms of $\Delta\varepsilon_{ij}^p$ and Δz, and summing all terms for $i = 1, ..., n$ we get

$$\Delta s_{ij} = \sum_{r=1}^{n} (1 - e^{-\alpha_r \Delta z}) \left[\frac{C_r}{\alpha_r} \frac{\Delta\varepsilon_{ij}^p}{\Delta z} - (s_{ij}^r)_{m-1} \right]. \tag{C-7}$$

Our goal is to determine the deviatoric stress increment Δs_{ij} corresponding to a given strain increment $\Delta\varepsilon_{ij}$. At this point, the deviatoric stress increment is known in terms of the plastic strain increment $\Delta\varepsilon_{ij}^p$ and the intrinsic time increment Δz. Therefore, we now look for an expression for the plastic strain increment $\Delta\varepsilon_{ij}^p$ and the intrinsic time increment Δ_z for a given strain increment $\Delta\varepsilon_{ij}$.

For a plastically incompressible material, the deviatoric stress increment Δs_{ij} can be written in terms of the plastic strain increment $\Delta\varepsilon_{ij}^{p}$ as

$$\Delta s_{ij} = 2G\,(\Delta e_{ij} - \Delta\varepsilon_{ij}^{p}), \qquad (C-8)$$

where e_{ij} is the deviatoric strain tensor, and G is the elastic shear modulus.

Combining the last two equations (C-7 and C-8), the plastic strain increment $\Delta\varepsilon_{ij}^{p}$ can be computed in terms of Δz for a given increment of deviatoric strain Δe_{ij} as

$$\Delta\varepsilon_{ij}^{p} = \frac{A_{ij}\Delta z}{B}, \qquad (C-9)$$

with

$$A_{ij}(\Delta z) = 2G\Delta e_{ij} + \sum_{r=1}^{n} (s_{ij}^{r})_{m-1}\,(1 - e^{-\alpha_r \Delta z}), \qquad (C-10)$$

and

$$B(\Delta z) = 2G\Delta z + \sum_{r=1}^{n} \frac{C_r}{\alpha_r}\,(1 - e^{-\alpha_r \Delta z}). \qquad (C-11)$$

At this point, we still need an expression for Δz. We approximate the equation defining the intrinsic time (C-2) as

$$\Delta z = (\Delta\varepsilon_{ij}^{p}\Delta\varepsilon_{ij}^{p})^{1/2}. \qquad (C-12)$$

By combining Eqs. (C-9) and (C-12), the intrinsic time increment is found to be the root of the following equation

$$B^2 - A_{ij}A_{ij} = 0. \qquad (C-13)$$

This non-linear algebraic equation is solved using a Newton-Raphson technique so that the increment Δz is computed for a given deviatoric strain increment Δe_{ij}. The plastic strain increment $\Delta\varepsilon_{ij}^{p}$ and $(s_{ij}^{r})_m$ can then be updated by Eqs. (C-9) and (C-6), respectively.

2. *Tangent Stiffness Matrix*

The plastic model described in the previous section is intended to be used as a part of a large finite element program to perform non-linear analysis. This requires the evaluation of a tangent stiffness matrix. In this section, we derive an expression for this matrix.

In what follows, we use the engineering notation and rewrite tensorial quantities in a vector form: $\Delta\boldsymbol{\sigma}$ denotes the vector of stress increments, i.e. $\Delta\boldsymbol{\sigma} = \{\Delta\sigma_{11}, \Delta\sigma_{22}, \Delta\sigma_{33}, \Delta\sigma_{23}, \Delta\sigma_{13}, \Delta\sigma_{12}\}^T$, $\Delta\mathbf{s}$ denotes the vector of deviatoric stress increments, i.e. $\Delta\mathbf{s} = \{\Delta s_{11}, \Delta s_{22}, \Delta s_{33}, \Delta s_{23}, \Delta s_{13}, \Delta s_{12}\}^T$, $\Delta\boldsymbol{\epsilon}$ denotes the vector of engineering strain increments, i.e. $\Delta\boldsymbol{\epsilon} = \{\Delta\varepsilon_{11}, \Delta\varepsilon_{22}, \Delta\varepsilon_{33}, 2\Delta\varepsilon_{23}, 2\Delta\varepsilon_{13}, 2\Delta\varepsilon_{12}\}^T$, $\Delta\boldsymbol{\epsilon}^e$ denotes the vector of engineering elastic strain increments, i.e. $\Delta\boldsymbol{\epsilon}^p = \{\Delta\varepsilon^e_{11}, \Delta\varepsilon^e_{22}, \Delta\varepsilon^e_{33}, 2\Delta\varepsilon^e_{23}, 2\Delta\varepsilon^e_{13}, 2\Delta\varepsilon^e_{12}\}^T$, while $\Delta\boldsymbol{\epsilon}^p$ denotes the vector of engineering plastic strain increments, i.e. $\Delta\boldsymbol{\epsilon}^p = \{\Delta\varepsilon^p_{11}, \Delta\varepsilon^p_{22}, \Delta\varepsilon^p_{33}, 2\Delta\varepsilon^p_{23}, 2\Delta\varepsilon^p_{13}, 2\Delta\varepsilon^p_{12}\}^T$.

The integration of the endochronic constitutive equation gave us a relation between deviatoric stresses and plastic strains (Eq. (C-7)) within an interval m. The "plastic" tangent stiffness matrix $\mathbf{C}^p$ is defined by

$$d(\Delta\mathbf{s}) = \mathbf{C}^p\, d\Delta(\boldsymbol{\epsilon}^p). \qquad (C-14)$$

Viewing $\Delta\mathbf{s}$ of Eq. (C-7) as a function of $\Delta\boldsymbol{\epsilon}^p$ and Δz, and differentiating with respect to $\Delta\boldsymbol{\epsilon}^p$ using the chain rule, the following expression for $\mathbf{C}^p$ is found [19] for the mth interval

$$\mathbf{C}^p = \frac{1}{\Delta z}\left[(P-Q)\frac{\mathbf{k}\,(\Delta\boldsymbol{\epsilon}^p)^T}{\Delta z} - \mathbf{R}\right]\mathbf{k}\,\Delta\boldsymbol{\epsilon}^p + Q\,\mathbf{k}, \qquad (C-15)$$

where

$$P = \sum_{r=1}^{n} C_r\, e^{-\alpha_r \Delta z}, \qquad (C-16)$$

$$Q = \frac{1}{\Delta z}\sum_{r=1}^{n}\frac{C_r}{\alpha_r}(1 - e^{-\alpha_r \Delta z}), \qquad (C-17)$$

$$\mathbf{R} = \sum_{r=1}^{n}\alpha_r\,(\mathbf{s}^r_{m-1})^T\, e^{-\alpha_r \Delta z}, \qquad (C-18)$$

$$\mathbf{k}=\begin{bmatrix} 1 & 0 & 0 & 0 & 0 & 0 \\ 0 & 1 & 0 & 0 & 0 & 0 \\ 0 & 0 & 1 & 0 & 0 & 0 \\ 0 & 0 & 0 & \frac{1}{2} & 0 & 0 \\ 0 & 0 & 0 & 0 & \frac{1}{2} & 0 \\ 0 & 0 & 0 & 0 & 0 & \frac{1}{2} \end{bmatrix}, \qquad (C-19)$$

and $\mathbf{s}^{r}_{m-1} = \{(s^{r}_{11})_{m-1},\ (s^{r}_{22})_{m-1},\ (s^{r}_{33})_{m-1},\ (s^{r}_{23})_{m-1},\ (s^{r}_{13})_{m-1},\ (s^{r}_{12})_{m-1}\}^{T}$.

The incremental relation between deviatoric stress and deviatoric plastic strain has been derived. We now want to express the deviatoric stress increment in terms of total strains. We can rewrite Eq. (C-14) as

$$\mathbf{S}\, d(\Delta\boldsymbol{\sigma}) = \mathbf{C}^{p}\, \mathbf{S}\, d(\Delta\boldsymbol{\epsilon}^{p}), \qquad (C-20)$$

where $\mathbf{S}$ is a 6×6 operator used to extract the deviatoric part of the vector of the stress increments $\Delta\boldsymbol{\sigma}$ and is given by

$$\mathbf{S}=\begin{bmatrix} 2/3 & -1/3 & -1/3 & 0 & 0 & 0 \\ -1/3 & 2/3 & -1/3 & 0 & 0 & 0 \\ -1/3 & -1/3 & 2/3 & 0 & 0 & 0 \\ 0 & 0 & 0 & 1 & 0 & 0 \\ 0 & 0 & 0 & 0 & 1 & 0 \\ 0 & 0 & 0 & 0 & 0 & 1 \end{bmatrix}. \qquad (C-21)$$

Note that for a plastically incompressible material, the hydrostatic part of the plastic strain tensor is zero so that $\mathbf{S}\, d(\boldsymbol{\epsilon}^{p}) = d(\boldsymbol{\epsilon}^{p})$.

From equation (C-8), the deviatoric differential stress increment is given in terms of the deviatoric strain differential increment by

$$\mathbf{S}\, d(\Delta\boldsymbol{\sigma}) = 2G\, \mathbf{k}\mathbf{S}\, d(\Delta\boldsymbol{\epsilon}^{e}). \qquad (C-22)$$

Eqs. (C-20) and (C-22) lead to:

$$\left[\frac{1}{2G}\mathbf{k}^{-1} + (\mathbf{C}^{p})^{-1}\right]\mathbf{S}\, d(\Delta\boldsymbol{\sigma}) = \mathbf{S}\left[d(\Delta\boldsymbol{\epsilon}^{e}) + d(\Delta\boldsymbol{\epsilon}^{p})\right], \qquad (C-23)$$

We now need to add the hydrostatic part of the stress tensor. We can write

$$\frac{1}{3K}\mathbf{H}\,d(\Delta\sigma)=\mathbf{H}\left[d(\Delta\epsilon^{e})+d(\Delta\epsilon^{p})\right], \tag{C-24}$$

where $\mathbf{H}$ is a 6×6 operator used to extract the hydrostatic part of the stress tensor and is given by

$$\mathbf{H}=\begin{bmatrix} 1/3 & 1/3 & 1/3 & 0 & 0 & 0 \\ 1/3 & 1/3 & 1/3 & 0 & 0 & 0 \\ 1/3 & 1/3 & 1/3 & 0 & 0 & 0 \\ 0 & 0 & 0 & 0 & 0 & 0 \\ 0 & 0 & 0 & 0 & 0 & 0 \\ 0 & 0 & 0 & 0 & 0 & 0 \end{bmatrix}. \tag{C-25}$$

Summing up the two parts of the stress tensor, we finally obtain from Eqs. (C-23) and (C-24), the differential elastoplastic stress-strain relation:

$$\begin{aligned} d(\Delta\sigma) &= \{3K\mathbf{H}+\left[\frac{1}{2G}\mathbf{k}^{-1}+(\mathbf{C}^{p})^{-1}\right]^{-1}\mathbf{S}\}\left[d(\Delta\epsilon^{e})+d(\Delta\epsilon^{p})\right] \\ &= \{3K\mathbf{H}+\mathbf{C}^{p}\left(\frac{1}{2G}\mathbf{k}^{-1}\mathbf{C}^{p}+\mathbf{I}\right)^{-1}\mathbf{S}\}\left[d(\Delta\epsilon^{e})+d(\Delta\epsilon^{p})\right] \\ &= \mathbf{E}\,d(\Delta\epsilon), \end{aligned} \tag{C-26}$$

where $\mathbf{I}$ is a 6×6 identity matrix.

Therefore, using the endochronic theory, the material property matrix $\mathbf{E}$ of the matrix for a given strain increment is given by:

$$\mathbf{E}=3K\mathbf{H}+\mathbf{C}^{p}\left(\frac{1}{2G}\mathbf{k}^{-1}\mathbf{C}^{p}+\mathbf{I}\right)^{-1}\mathbf{S}, \tag{C-33}$$

where $\mathbf{C}^{p}$ is given by Eq. (C-15).

Vita

Lucie Parietti was born in Laxou, France on March 13, 1969. She acquired her B.S degree in Material & Structural Engineering from the *Ecole Polytechnique Féminine*, France in 1992.

After graduation, she plans to work in the industry as a project engineer.